A domain-swapped CaMKII conformation facilitates linker-mediated allosteric regulation

Bao V. Nguyen*[1,2,3], Can Özden*[1,3], Kairong Dong[1,4], Ana P. Torres-Ocampo[1,2], Noelle Dziedzic[1,2], Daniel Flaherty[3], Jian Huang[4], Saketh Sankura[3], Nikki Lyn Abromson[3], Diana R. Tomchick[5,6], Jianhan Chen[4], Scott C Garman[3], Margaret M Stratton[‡3]

*These authors contributed equally
[‡] Corresponding author. Email: mstratton@umass.edu

[1] Molecular and Cellular Biology Graduate Program, University of Massachusetts, Amherst, MA 01003, USA. [2] Chemistry-Biology Interface Training Program, University of Massachusetts, Amherst, MA 01003, USA. [3] Department of Biochemistry and Molecular Biology, University of Massachusetts, Amherst, MA 01003, USA. [4] Department of Chemistry, University of Massachusetts, Amherst, MA 01003, USA. [5] Department of Biochemistry, University of Texas Southwestern Medical Center, Dallas, TX, USA,[6] Department of Biophysics, University of Texas Southwestern Medical Center, Dallas, TX 75390, USA.

ABSTRACT

Ca^{2+} signaling plays a key role in physiological processes such as memory formation and cardiac function. Ca^{2+}/calmodulin-dependent protein kinase II (CaMKII) is the primary kinase that responds to Ca^{2+} inputs in these cells. There are four CaMKII paralogs in mammals which are alternatively spliced in the variable linker region to create upwards of 70 different variants. In this study, we systematically studied different linker regions and determined that the position of charged residues within the linker region modulates the Ca^{2+}/CaM sensitivity of the holoenzyme. We present an X-ray crystal structure of full-length CaMKIIδ that shows a domain-swapped conformation of the subunits within the dodecameric holoenzyme. In this structure, the kinase domain of one subunit is docked onto the hub domain of a different subunit, providing an additional interface within the holoenzyme. Mutations at the equatorial and lateral interfaces revealed that the kinase-hub interaction dissociates as the hub-hub interfaces are disturbed, which led alterations in the stoichiometry of CaMKII holoenzyme and Ca^{2+}/CaM sensitivity. Molecular dynamics simulations of linker-containing domain-swapped and non-domain-swapped CaMKIIs reveal that the domain-swapped configuration facilitates an interaction between the calmodulin binding domain and the variable linker region, such that dynamic electrostatic forces between charges on these segments can modulate the equilibrium between the compact and extended conformational states of the holoenzyme. Small angle X-ray scattering data confirms that a negatively charged linker CaMKII holoenzyme adopts a more compact conformation compared to a positively charged linker. These data support a model where patches of charged linker residues interact with the calmodulin binding domain to allosterically regulate sensitivity to Ca^{2+}/CaM. Our findings provide a new framework for understanding CaMKII structure and allosteric regulation by the variable linker region in Ca^{2+}-sensitive cells.

INTRODUCTION

Ca^{2+}/calmodulin-dependent protein kinase II (CaMKII) is critical for signaling during long-term memory formation, fertilization, and cardiac pacemaking. There are four CaMKII genes (α, β, δ, γ) that are expressed differentially throughout the body, where CaMKIIα and β are neuronal, CaMKIIγ is in muscle tissue, eggs and sperm, and CaMKIIδ is expressed in cardiomyocytes. All CaMKIIs share the same domain organization: an N-terminal kinase domain, regulatory

segment, variable linker region, and C-terminal hub domain (oligomerization domain). The rise of intracellular Ca^{2+} concentration is sensed by calmodulin (CaM) to form a Ca^{2+}/CaM complex, which competitively binds the CaMKII regulatory segment thereby relieving inhibition of the substrate binding site on the kinase domain. The hub domain is responsible for the oligomerization of dodecameric (Chao *et al.*, 2011), tetradecameric (Hoelz *et al.*, 2003; Bhattacharyya *et al.*, 2016; McSpadden *et al.*, 2019; Sloutsky *et al.*, 2020), and hexadecameric CaMKII holoenzymes (Özden *et al.*, 2024).

The kinase and the hub domains are connected by a variable linker region. The four CaMKII paralogs have many splice sites in the linker region, creating upwards of 70 possible variants expressed (Sloutsky *et al.*, 2020). The linker sequence and length are variable, spanning from zero (*i.e.*, no linker) to 217 residues, and affording them different biophysical properties and post-translational modifications (Tombes *et al.*, 2003; Sloutsky and Stratton, 2020). Previous studies have shown that the linker length can modulate Ca^{2+}/CaM sensitivity of CaMKIIα, but not CaMKIIβ (Bayer *et al.*, 2002; Chao *et al.*, 2011; Sloutsky *et al.*, 2020). Detailed mechanistic insight into the regulatory role of specific linker regions on CaMKII function and regulation has been lacking. While many structures of CaMKII kinase and hub domains as isolated domains have been determined (Stratton *et al.*, 2013; Bhattacharyya *et al.*, 2020), they do not visualize the linker region, which is presumed to be mostly disordered. The first structure of the intact CaMKIIα holoenzyme with no linker (CaMKIIα-0) revealed a new conformation (deemed compact or closed), where the kinase domain docked onto the hub domain of the same subunit (Chao *et al.*, 2011). This crystal structure provided a clear explanation for biochemical observations that CaMKIIα-0 requires a high concentration of Ca^{2+}/CaM for activation.

Small angle X-ray scattering (SAXS) and cryo-electron microscopy (cryo-EM) have been employed to assess the structure of CaMKIIα with a 30-residue linker (CaMKIIα-30), which activates more easily, at lower concentrations of Ca^{2+}/CaM. SAXS showed a significant difference between CaMKIIα-0 and CaMKIIα-30, where CaMKIIα-30 had a larger envelope, indicating that the kinases were farther from the hub instead of docked as seen in CaMKIIα-0 (Chao *et al.*, 2011). Cryo-EM showed that subunits within a CaMKIIα-30 complex did adopt a closed conformation, but not all subunits as seen in the CaMKIIα-0 structure (Sloutsky *et al.*, 2020). These results imply that extending the linker length increases flexibility, but still allows an equilibrium between compact and extended states.

Biochemical and structural data have led to a model for CaMKIIα where longer linkers increase kinase flexibility farther from the hub domain (extended conformation), increasing accessibility to Ca^{2+}/CaM (Chao *et al.*, 2011). Shorter linkers (*i.e.*, no linker) reduce kinase flexibility leading to a stronger interaction between the kinase and hub domains (compact conformation), decreasing accessibility to Ca^{2+}/CaM. Here, we further examined whether the sequence of the linker region also impacts Ca^{2+}/CaM sensitivity. We employed a combination of biochemistry, SAXS, X-ray crystallography, and molecular dynamics (MD) simulations to better understand our biochemical results in light of CaMKII conformation and regulation. We present the structure of an intact CaMKIIδ holoenzyme, which reveals an unambiguous domain-swapped dimer conformation. In the context of this new structure combined with MD simulations, we propose a model for how the linker sequence, composition, and orientation affect the accessibility of the Ca^{2+}/CaM binding site to dictate CaMKII sensitivity to calcium.

RESULTS

The variable linker sequence affects Ca^{2+}/CaM sensitivity

We hypothesized that the composition of the linker region, in addition to its length, could directly modulate the sensitivity of CaMKII to Ca^{2+}/CaM. To test this, we changed the linker sequence in CaMKIIα but maintained similar lengths and compared this to other variants: CaMKIIβ and CaMKIIδ (both 95% similar to CaMKIIα). All CaMKII variants encode exons 14 and 18 in the genetic background. CaMKIIα has the shortest encoded variable linker region, which only includes exons 14, 15, and 18 (Sloutsky *et al.*, 2020) (**Fig. 1A**). Exons 14 and 18 are similar lengths, comprised of 14 and 16 residues, respectively, but have different sequences (**Fig. 1B**). We constructed variants of CaMKIIα, β, and δ containing only exon 14 or only exon 18 as the linker region from the corresponding genetic sequence (i.e. CaMKIIα with α exon 14, etc.). For all variants, inclusion of exon 14 significantly increased the Ca^{2+}/CaM sensitivity compared to variants containing exon 18. CaMKII variants containing just exon 14 had EC_{50} values ~20 nM whereas variants containing just exon 18 had EC_{50} values ranging from 91 – 193 nM (**Fig. 1C-E**). CaMKIIα displayed the largest shift in EC_{50} value, from 17 nM to 193 nM, so we performed further experiments using CaMKIIα.

Phosphorylation of the variable linker does not account for difference in Ca^{2+}/CaM sensitivity

There are two striking differences in the sequences of exons 14 and 18. One is the number of potential autophosphorylation sites, and the second is the net charge (**Fig. 2A**). We first tested whether autophosphorylation shifts the EC_{50} by performing phosphoproteomic analysis of CaMKIIα upon incubation with ATP/Mg^{2+} and Ca^{2+}/CaM for 1 minute at room temperature. Peptides were analyzed using LC/MS/MS and showed that all Ser and Thr residues on exon 18 were autophosphorylated under these conditions *in vitro* (**Fig. S1A-F**). We created a CaMKII mutant with all Ser and Thr residues in exon 18 mutated to Ala (S/TΔA mutant). If phosphorylation played a role in causing the increased sensitivity, we would expect this mutant to be left-shifted compared to WT exon 18. Instead, this non-phosphorylatable mutant required more Ca^{2+}/CaM for activation (EC_{50} = 350 ± 25 nM) compared to WT exon 18 (**Fig. S1G**). From these data, we concluded that although these residues can be phosphorylated *in vitro*, this is not why inclusion of exon 18 makes it more difficult to bind Ca^{2+}/CaM. For the subsequent experiments, we used the S/TΔA mutant to remove the confounding variable of autophosphorylation of the linker unless stated otherwise.

The position of charge on the variable linker regulates Ca^{2+}/CaM sensitivity

We next tested the effect of net charge on Ca^{2+}/CaM binding. All net charges were calculated at pH 7.5. Exon 14 is highly basic (net charge +3) and exon 18 is highly acidic (net charge -5) (**Fig 2A**). If the net charge is driving this effect, then the inclusion of a basic exon makes it easier to activate CaMKII, while the inclusion of an acidic exon would make it harder to activate CaMKII. We converted exon 14 from basic to acidic by mutating all basic residues to acidic residues (**Fig 2A**). We hypothesized that including acidic exon 14 would make it harder to activate CaMKII. Indeed, acidic exon 14 has a right-shifted EC_{50} (102 ± 8 nM) compared to WT exon 14 (43 ± 3 nM) (**Fig 2B**). Similarly, we converted exon 18 from acidic to basic and this resulted in a left-shifted EC_{50} (34 ± 3 nM) compared to the WT exon 18 (201 ± 25 nM) (**Fig 2C**). To test whether the charge positioning has an effect, we created a mutant where the sequence of exon 18 was reversed. This mutant left-shifted the EC_{50} value (41 ± 2 nM) compared to WT exon 18 (108 ± 6 nM) (**Fig 2D**), indicating that the position of the charges does impact the accessibility of the regulatory segment to Ca^{2+}/CaM. To further interrogate this positional effect, we compared six

combinations of exons 14 and 18 within CaMKIIα (**Fig 2E**). For reference, CaMKIIα with exons 14 and 18 included [CaMKII (14,18)] is the most prevalent CaMKII variant in the brain (Sloutsky *et al.*, 2020). CaMKIIα mutants with basic exon 14 positioned proximal to the regulatory segment have left-shifted EC_{50} values (~20 nM), whereas all mutants with acidic exon 18 in this position have right-shifted EC_{50} values (~70 nM) (**Fig 2F**).

Alterations in the linker change the compactness of the holoenzyme

We used small-angle x-ray scattering (SAXS) which has previously been implemented to study conformational differences in CaMKII variants (Rosenberg *et al.*, 2005; Chao *et al.*, 2011; Sloutsky *et al.*, 2020). We performed SAXS coupled with size exclusion chromatography and multi-angle scattering and observed a single elution peak for each sample (**Figs. 3A, B**). Guinier analyses (**Figs. 3C, D**) revealed a significant difference in the radius of gyration (ANCOVA, $F_{1,38}$ = 173.86, p <0.001) between α Exon 18 (R_g = 60 ± 1 Å) and α Exon 14 (R_g = 68 ± 2 Å). In addition, the maximal dimensions derived from pair-wise distribution functions also showed a substantial difference between α Exon 18 (D_{max} = 190 Å) and α Exon 14 (D_{max} = 257 Å) (**Fig. 3E**). These data suggest that inclusion of α exon 18 results in more compact holoenzymes compared to α exon 14-containing holoenzymes.

The CaMKII holoenzyme is comprised of domain-swapped dimers

We determined the X-ray crystal structure of full-length human CaMKIIδ (residues 10-447) with no variable linker to 2.3 Å (**Table 1**). The crystallized protein contained one substitution (D336C), introduced for labeling experiments, which is surface exposed and does not make any subunit contacts. The structure was resolved to contain three CaMKII subunits in the asymmetric unit, which generates a dodecameric holoenzyme by the crystallographic $4_2 22$ symmetry (**Fig. 4A, Fig. S2**). This overall architecture is identical to that of CaMKIIα with no linker (PDB: 3SOA (Chao *et al.*, 2011)). However, the improved resolution and the different space group allowed for unambiguous building of residues 300-313, which includes the junction between the regulatory segment and hub domain herein deemed the 'connector segment' (**Fig. S2A**). The electron density in this region extends away from the kinase domain of one subunit toward the hub domain of the opposite stacked ring, resulting in a domain-swapped dimer with the kinase domain of one subunit associates with the hub domain of a copy across a molecular 2-fold axis (**Fig. 4A, B**). The CaM footprints of the domain-swapped dimer run antiparallel to one another and are in extensive contact (**Fig. 4B**).

The hub:hub interfaces that drive oligomerization are equatorial and lateral interfaces with extensive hydrophobic interactions and hydrogen bonding (**Fig. 5A**). We rationally designed interfacial mutations to validate the structure and to drive oligomer dissociation. We compared full-length CaMKIIδ constructs with no variable linker region (our crystallization construct) with mutations at the lateral and/or equatorial hub interfaces and employed mass photometry to measure the masses of single particles.

WT CaMKIIδ holoenzymes form dodecameric oligomers (600 kDa) from 100 nM to 12.5 nM (the lowest concentration we can reliably detect), which is consistent with our crystal structure (**Fig. 5B**, **Fig. S3**). In the WT sample, we tested F368A (F367A in CaMKIIα numbering), which has previously been shown to destabilize the oligomer (Bhattacharyya *et al.*, 2016). We found that F368A CaMKIIδ holoenzymes form predominantly tetradecameric oligomers (700 kDa) (**Fig. 5B**). At 100 nM, we observed ~10% of the total population as dimers (100 kDa) and ~5% as tetramers (200 kDa) (**Fig. S3**). This percentage of dimers increases to ~30% at our lowest concentration tested (12.5 nM). Compared to WT which has negligible small species across the

concentration range tested (<7% monomer/dimer), F368A destabilizes the oligomer to form dimers at low concentrations.

To enhance dimerization at higher concentrations, we employed a second mutation in addition to F368A. Both L405 and Q407 pack against the neighboring hub subunit along the lateral interface (**Fig. 5A**). The double mutants (F368A/L405M and F368A/Q407A) produced a predominant dimer population (100 kDa) from 100 nM to 12.5 nM (**Fig. 5B**, **Fig. S3**). There was ~5% tetradecameric holoenzyme (700 kDa) at 100 nM, but this disappeared below 75 nM (**Fig. S3**). Finally, to create a monomeric population, we introduced mutations at the equatorial interface (C399R and H439R). The double mutant C399R/H439R produced a monomeric population (50 kDa) (**Fig. 5B**, **Fig. S3**). In these distributions, there is a considerable shoulder which is likely some dimeric contribution (**Fig. S3**).

The domain-swapped conformation suggests that the interaction between the hub domain and the kinase domain could stabilize the dimer across the equatorial plane. To test this, we introduced an additional C399R mutation to the F368A background to disrupt both lateral and equatorial interfaces while leaving the kinase-hub interface intact. The resulting F368A/C399R mutant behaves similarly to the H439R/C399R mutant, which all predominantly monomers at concentrations lower than 50 nM (**Fig. 5B**, **Fig. S3**). The molecular weight distributions of F368A/C399R and H439R/C399R mutants also show skewness to the right with a shoulder visible around 80 kDa, suggesting an equilibrium between monomers and most likely dimers which results in an apparent molecular weight of ~65 kDa at concentrations above 75 nM (**Fig. 5B, Fig. S3**). This indicates that the kinase-hub interaction dissociates with hub dissociation.

We next determined the functional implication of oligomerization on CaMKII activation. We measured the activity of CaMKIIδ oligomer mutants at varying Ca^{2+}/CaM concentrations towards syntide-2, as has been done previously (Chao *et al.*, 2010, 2011; Sloutsky *et al.*, 2020). We observed that all CaMKIIδ constructs at final concentration of ~13 nM exhibited positive cooperativity ranging from 1.7 to 2 regardless of the oligomeric state (**Fig. S4**). The EC_{50} values for the CaMKIIδ mutants were left shifted compared to the WT (**Fig. S4**). The dimeric mutants (F368A/L405M and F368A/Q407A) and monomeric mutants (F368A/C399R and C399R/H439R) had a 2-fold lower EC_{50} value compared to WT CaMKIIδ (EC_{50} = 80 ± 4 nM). The tetradecameric mutant (F368A) showed an intermediate sensitivity toward Ca^{2+}/CaM (EC_{50} = 61 ± 4 nM) relative to the other mutants and the wildtype. These results demonstrated that the oligomeric state of CaMKII does tune Ca^{2+}/CaM sensitivity.

The domain-swapped dimer conformation orients electrostatic interactions by the linker region to influence autoinhibition

There are six basic residues in the CaM binding region of the regulatory segment (CaMKIIδ residue number, K^{292}KFNAR^{297}RKLK^{301}), four of which (blue) are involved in electrostatic interactions with Ca^{2+}/CaM (Rellos *et al.*, 2010). We hypothesized that the negatively charged residues of the linker region could interact with the positively charged residues of the calmodulin binding region, which would reduce the affinity of calmodulin binding. To interrogate this, we employed molecular dynamic (MD) simulations paired with experimental validations by mutagenesis. We first modeled linker regions comprised of either WT exon 14, WT exon 18, or reversed exon 18 in the domain-swapped conformation of a CaMKIIδ construct that contains two kinase domains and four hub domains (**Fig. S5**). This construct captures the complete kinase-hub and kinase-kinase domain interactions of the dodecamer. The initial linker conformations were generated using a no-linker construct, which was also simulated for comparison (**Fig. S5**). All constructs remain stable throughout the simulation timescale (**Fig.**

S6), which is expected as the holoenzyme should remain in an autoinhibited state. Analysis of dynamic fluctuations however revealed significant differences in key regions. While the root-mean-squared fluctuation (RMSF) of all hub domains showed very similar and low magnitudes (**Fig. S7**), the RMSF of the kinase domain and regulatory segment from exon 14 or reversed exon 18 constructs are larger compared to those with no linker or exon 18 (**Fig. S7**). The implication is that there is more flexibility in the regulatory segment when exon 14 or reversed exon 18 are incorporated compared to lower flexibility with no linker or exon 18. This would explain the contrasting effects of these linkers on Ca^{2+}/CaM sensitivity (see **Fig. 2**). We also ran simulations of these same linker constructs in the non-domain-swapped conformation (PDB: 3SOA), and there were no significant differences in RMSF throughout the structure between different linker constructs (**Fig. S8**).

In-depth pairwise residue interaction analyses indicated that the N- and C-terminal negative charges of exon 18 are in proximity to Lys 301 and Arg 297, which are involved in Ca^{2+}/CaM binding (Rellos *et al.*, 2010). The negative charges on the N-terminus of exon 18 may contribute more because they were <5 Å away from Lys 301 and Arg 297 over the 200 ns trajectory (**Fig. 6A-D**, **Fig. S9**). To test the contribution of the N-terminal negative charges, we introduced EΔQ and DΔN mutations to exon 18 (**Fig. 6D**). Removing two negative charges in the N-terminus of exon 18 reduced the EC_{50} by half, whereas removing two negative charges at the C-terminal end did not change the EC_{50} significantly. Pairwise analyses showed the negative charges on the C-terminus of exon 18 had less frequent contacts with the positive charges of the regulatory segment (**Fig. S10**). Mutating all acidic residues on exon 18 made the variant (Exon 18 mut3) significantly more sensitive to Ca^{2+}/CaM (**Fig. 6E**).

We next asked if a similar charge distribution can be applied to other linker sequences. Exon 14 has positive charges distributed across the sequence. We gradually increased the negative charge at the C-terminal portion of exon 14 (**Fig 6F**), which resulted in a negligible change in Ca^{2+}/CaM sensitivity. Then, we mutated the first Lys of exon 14 to Glu (Exon 14 mut3), and observed a significant increase in Ca^{2+}/CaM sensitivity relative to WT exon 14 (**Fig. 6G**). Adding more negative charge to the C-terminus did not further right-shift the EC_{50} (Exon 14 mut4) (**Fig. 6G**). These observations are consistent with the mechanism that the domain-swapped conformation of CaMKII positions the N-terminal negative charges of the linker to interact with positively charged residues of the calmodulin footprint, therefore regulating the accessibility of the regulatory segment. Negative charges at the C-terminal end had a more modest effect on sensitivity regulation.

DISCUSSION

The structure of CaMKIIδ-0 provides the first evidence for a domain-swapped conformation within the holoenzyme. The previous structure of CaMKIIα-0 (PDB: 3SOA) (Chao *et al.*, 2011) had ambiguous density in the connector segment and was interpreted with neighboring kinase and hub domains from the same polypeptide chain. We were able to observe the domain-swapped conformation due to a higher resolution of the residues that connect the kinase to the hub domain (CaMKIIα 299-304 and 309-314). Additionally, our structure provides three independent views of the connector segment from the three chains in the asymmetric unit (A, B, C, **Fig. S2A**). Each chain showed electron density that is only consistent with a domain-swapped dimer. The domain-swapping results in residues 307-315 running antiparallel to one another. Although we achieved higher resolution, the B-factors for residues 310-313 are relatively high (~93 to 143 for Cα), likely indicating more flexibility in this region (**Fig. S2B**). Region is likely to be flexible because there is weak density and high B-factors, as might be

expected for a junction between domains. Many domain-swapped oligomers contain flexible linkers to accommodate this conformation (Gronenborn, 2009; Rousseau *et al.*, 2013)

A domain-swapped conformation of CaMKII has several implications. As tested here, the orientation of the linker region to the Ca^{2+}/CaM binding site provides an opportunity for the linker to regulate the accessibility of Ca^{2+}/CaM binding. Domain-swapping increases the number of communication points between subunits, which in turn, provides a larger landscape for allosteric effects such as cooperativity (Chao *et al.*, 2010) and hub regulation of sensitivity (Chao *et al.*, 2011; Sloutsky *et al.*, 2020). This new perspective on the CaMKII holoenzyme structure necessitates interpreting biochemical and structural data in light of domain-swapping.

In 2000, Kwiatkowski and McGill showed that substituting a basic residue with an acidic one in the first linker exon of CaMKIIγ (R318E) increased the EC_{50} for Ca^{2+}/CaM, consistent with our results (Kwiatkowski and McGill, 2000). Our study aimed to make direct comparisons by using linker exons that are mostly conserved across paralogs (combinations of exons 14 and 18). However, it is important to note that the CaMKIIα variants we tested, containing only exon 14 or exon 18, have not been observed in cells (Tombes *et al.*, 2003; Cook *et al.*, 2018; Sloutsky *et al.*, 2020). Additionally, incorporation of exon 14 or 18 alone may be less likely because they do not contain complete codons (i.e., not a multiple of three) (Sloutsky and Stratton, 2020). Nevertheless, our comparisons allowed us to build a model where sensitivity is at least partially dependent on the distribution of charged residues in the linker, specifically the linker region most proximal to the regulatory segment. The model we provide fits the data for the set of variants we have tested here, however, because of the enormous diversity of CaMKII variants due to alternative splicing, we may need to expand this model to comprehensively explain the intricate dynamics of the autoinhibited state (Gaertner *et al.*, 2004). Because we have concluded that the linker region most proximal to the regulatory segment is sufficient for influencing sensitivity, it may only be necessary to consider this part of the linker. Future efforts will focus on testing a broader range of variants to refine this model.

Charged residues in the CaMKII linker have been implicated in disease. Researchers have identified K323N or K328E mutations in CaMKIIα linker in patients with dementia (Wang *et al.*, 2017). These mutants were found to impair Ca^{2+}/CaM binding and autophosphorylation at T286, resulting in reduced CaMKII binding to NR2B subunit of the ionotropic NMDA receptor, which is consistent with our findings here (Wang *et al.*, 2017). Additionally, another study demonstrated that phosphorylation at S331 in CaMKIIα effectively inhibited CaMKII and led to an enhancement of memory-based addiction treatment outcomes (Rich *et al.*, 2016). Indeed, CaMKIIα S331E had decreased activity compared to WT or S331A (Rich *et al.*, 2016). While our mass spectrometry analysis detected phosphorylation at S330, phosphorylation on exon 18 was insufficient to explain our observed shift in Ca^{2+}/CaM sensitivity (**Fig. S1G**). Previous research has also suggested that the charge of the linker region, whether through phosphorylation or insertion of charged residues by alternative splicing, influences localization and interaction with binding partners (Heist *et al.*, 1998; O'Leary *et al.*, 2006; Kim *et al.*, 2015). Future studies will investigate the role of linker phosphorylation in CaMKII sensitivity, while also considering the potential impact of other post-translational modifications such as methylation and ubiquitination.

CaMKII structure and regulation are intimately linked. The CaMKII holoenzyme adopts an autoinhibited state in the absence of Ca^{2+}, and the strength of autoinhibition relies on the sequence of the hub domain (Sloutsky *et al.*, 2020) as well as the length (De Koninck and Schulman, 1998; Bayer *et al.*, 2002; Chao *et al.*, 2011; Sloutsky *et al.*, 2020) and distribution of charge of the linker region, as shown here. Recent studies suggest that understanding CaMKII regulation requires consideration of its non-enzymatic scaffolding role (Chen *et al.*, 2023; Tullis

et al., 2023) in addition to its kinase activity. While our focus has been on CaMKII activity, it is worth noting that this is also tied to its scaffolding function, which necessitates phosphorylation at T286. Enhanced CaMKII activation may improve kinetics for scaffolding capabilities.

CaMKII is required for signaling in neurons, oocytes, and cardiomyocytes – all cells that use Ca^{2+} oscillations for communication. The responsiveness of CaMKII to Ca^{2+} is dictated by its structure, where stronger autoinhibition decreases sensitivity to Ca^{2+}. Our results add to this picture by now incorporating the sequence of the variable linker region as an additional regulatory component. While each cell likely expresses a distinct set of splice variants of CaMKII paralogs, there is no data on protein levels at single-cell resolution. Knowing the abundance of all expressed CaMKIIs would provide testable hypotheses on the cellular response to Ca^{2+} and its variations across different cells and tissues.

Acknowledgements
We thank Dr. Luke Chao for his helpful comments on the manuscript. We thank Dr. Vincent Tagliabracci for beamline assistance. We thank Dr. Steve Eyles and the Mass Spectrometry core for helping with mass spectrometry samples. SAXS work was conducted at the Advanced Light Source (ALS), a national user facility operated by Lawrence Berkeley National Laboratory on behalf of the Department of Energy, Office of Basic Energy Sciences, through the Integrated Diffraction Analysis Technologies (IDAT) program, supported by DOE Office of Biological and Environmental Research. Additional support comes from the National Institute of Health project ALS-ENABLE (P30 GM124169) and a High-End Instrumentation Grant S10OD018483. Crystallographic data shown in this report are derived from work performed at the Argonne National Laboratory, Structural Biology Center at the Advanced Photon Source. SBC-CAT is operated by UChicago Argonne, LLC, for the US Department of Energy, Office of Biological and Environmental Research under contract DE-AC02-06CH11357. This work was supported in part by NIH grant to M.M.S. (NIH R35GM145376), NIH grant to J.C. (NIH R35GM144045), a fellowship from the University of Massachusetts as part of the Chemistry-Biology Interface Training Program (National Research Service Award T32 GM139789) to V.C.B.N., J.H., N.D., and A.P.T.-O.

METHODS

Plasmid construction

cDNAs encoding full-length CaMKII variants were subcloned into a pSMT3 vector containing N-terminal 6×His followed by a SUMO tag. The DNA sequences of exon 14 and exon 18 contain incomplete codons for all CaMKII genes tested in this study. To clone exon 18, we remove the last nucleotide from the last exon (exon 12) of the regulatory segment immediately preceding the linker region, which results in no changes in the protein sequences of the regulatory segment and exon 18. To clone exon 14, we added one or two nucleotides to the 3'-end of exon 14 to keep the sequence in frame of translation without changing the amino acid sequence. The DNA sequences of exon 14 and exon 18 are shown below. Added nucleotides are underlined.

α Exon 14: GAGGGAAGAGTGGGGGAAACAAGAAGAGCGATGGTGTGAAGG
α Exon 18: GGAATCCTCAGAGAGCACCAACACCACCATCGAGGATGAAGACACCAAAG
β Exon 14: CGGCCAAGAGCCTGCTGAATAAGAAGGCCGACGGCGTGAAGG
β Exon 18: GAGAGCAGTGACAGCGCCAACACCACAATTGAGGATGAGGACGCCAAGG
δ Exon 14 CCGCCAAGAGCCTGCTGAAGAAACCGGATGGCGTGAAGG
δ Exon 18: GAAAGCACCGAGAGTAGCAATACCACCATCGAAGACGAGGATGTGAAGG

Protein expression and purification
Rosetta 2(DE3)pLysS competent cells (Millipore) were used to recombinantly express all CaMKII variants as previously described (Sloutsky *et al.*, 2020). CaMKII variants were cotransformed with lambda phosphatase, and overnight expression was done by 1 mM IPTG (GoldBio) in 18 °C shaker. Cell pellets were resuspended and lysed in Buffer A [25 mM Tris-HCl (pH 8.5), 150 mM KCl, 50 mM imidazole, 10% glycerol; Sigma] with protease inhibitor mixture [0.2 mM AEBSF, 5.0 μM leupeptin, pepstatin (1 μg/ml), aprotinin (1 μg/ml), trypsin inhibitor (0.1 mg/ml), 0.5 mM benzamidine] and DNase (1 μg/ml) (Sigma). Protein purification was performed using ÄKTA pure chromatography system at 4°C. Modifications in the ionic strength and buffer pH were applied if necessary. After pelleting the cell debris, clarified cell lysate was loaded onto one or two 5-ml HisTrap FF NiNTA Sepharose column (GE) and eluted with a combination of 50% buffer A and 50% buffer B [25 mM tris-HCl (pH 8.5), 150 mM KCl, 1 M imidazole, 10% glycerol] for a final concentration of 0.5 M imidazole. Residual imidazole was separated from the protein using a HiPrep 26/10 Desalting column, and His SUMO tags were cleaved with Ulp1 protease overnight at 4°C in buffer C [25 mM Tris-HCl (pH 8.5), 150 mM KCl, 2 mM TCEP (GoldBio), 50 mM imidazole, 10% glycerol]. Cleaved tags were separated by a subtractive NiNTA step. Next, an anion exchange step was performed with a 5-ml HiTrap Q-FF or Mono Q™ 10/100 GL and protein was eluted with a KCl gradient. Eluted proteins were concentrated and further purified in gel filtration buffer [25 mM tris-HCl (pH 8.0), 150 mM KCl, 1 mM TCEP, 10% glycerol] using a Superose 6 Increase 10/300 size exclusion column. Pure fractions were then concentrated, aliquoted, flash-frozen in liquid nitrogen, and stored at −80°C until further use. All columns were purchased from GE.

Calmodulin (*Gallus gallus*) was recombinantly expressed from a pET-15b vector (a gift from A. Nairn, Yale School of Medicine) in BL21(DE3) cells (Millipore) and purified as previously described (Stratton *et al.*, 2014; Sloutsky *et al.*, 2020). The concentration of CaM stock was measured in triplicate by circular dichroism using Jasco J-1500 spectrophotometer scanning a wavelength spectrum between 260 and 205 nm. The characteristic wavelength of 222 nm was used in the calculation of calmodulin concentration as follows:

$$[\text{calmodulin}](\text{mM}) = \frac{1000 \times (CD_{Sample}^{222\,nm} - CD_{Blank}^{222\,nm})}{\Theta \times l \times \text{number of residues}}$$

where the circular dichroism at 222 nm (CD^{222nm}) is expressed in mdeg, Θ is the molar residual ellipticity (158000 deg cm^2 $dmol^{-1}$ $residue^{-1}$), and *l* is the path length in cm.

Couple Kinase Assay
Kinase activity was monitored by Synergy H1 microplate reader (BioTek) at 30 °C as previously described with minor modifications (Stratton *et al.*, 2014; Sloutsky *et al.*, 2020). Each reaction in the plate contained varying concentrations of calmodulin and a master mix solution with the following components at final concentrations: 25 mM Tris (pH 7.5; Thermo Fisher Scientific), 150 mM KCl (Sigma), Tris/$MgCl_2$ buffer (50 mM/10 mM, respectively) (Thermo Fisher Scientific), 0.2 mM $CaCl_2$ (Sigma), 1 mM phosphoenolpyruvate (Alfa Aesar), nicotinamide adenine dinucleotide (0.15 mg/ml; Sigma), pyruvate kinase (10 U/ml; Sigma), lactate dehydrogenase (30 U/ml; Millipore Sigma), 2 mM adenosine triphosphate (ATP) (Sigma), and 0.3 mM syntide (LifeTein). The final pH of the reaction was 7.5-8, and the reaction was initiated with CaMKII for a final concentration of 13.3 nM (as monomer concentration). Absorbance of NADH was monitored at 15-s intervals for 10 min. The changes in the absorbance for each reaction over time were measured by calculating the slope of a five-point sliding window (1 min 15 s), and the maximum observed slope was used as the observed kinetic rate of that reaction. Kinetic rates across the calmodulin titration were fitted with Hill equation as shown below (Prism) to obtain

the EC_{50} (defined as the calmodulin concentration needed to reach the half-maximal reaction velocity) and Hill coefficient values (h).

$$y = V_{min} + V_{max} * \frac{x^h}{EC_{50}^h + x^h}$$

Small-Angle X-ray Scattering

SAXS data were collected via mail-in service at the Advanced Light Source in Berkeley beamline 12.3.1. For high-throughput SAXS experiment (Hura *et al.*, 2009), 30 uL of samples at three different concentrations ranging from 1 mg/mL to 8 mg/mL were prepared in the matching gel filtration buffer. Incident wavelength was set at λ = 1 Å at a sample-to-detector distance of 1.5 m, resulting in scattering vectors (q) ranging from 0.011 to 0.435 $Å^{-1}$. Data were collected with Pilatus3 2M pixel array detector (Dectris) over 10 sec with 0.3 s exposure times, resulting in 33 frames which were then buffer-subtracted and processed in Frameslice (https://bl1231.als.lbl.gov/ran). All data were collected at room temperature (18–21 °C). SAXS profiles from different concentrations were merged and analyzed for the values of radius of gyration (R_g) and D_{max} in BioXTAS RAW (Hopkins *et al.*, 2017).

For SAXS analyses coupled with multi-angle light scattering in-line with size exclusion chromatography (SEC-SAXS-MALS), samples at concentrations from 3 to 10 mg/mL were prepared in SEC buffer [25 mM tris-HCl (pH 8.8), 250 mM KCl, 1 mM TCEP, 2% glycerol] and kept frozen in -20 °C until the run session. X-ray wavelength was set at λ=1.127 Å at a sample-to-detector distance of 2.1 m, resulting in q ranging from 0.011 to 0.473 $Å^{-1}$. The scattering vector is $q = 4\pi\sin\theta/\lambda$, where 2θ is the scattering angle. Size exclusion chromatography was performed using an Agilent 1260 series HPLC with a Shodex PROTEIN KW-804 column equilibrated in SEC buffer at a flow rate of 0.65 mL/min. 55 uL of each sample was applied to the SEC system and split 3-to-1 ratio between SAXS flow cells and a series of UV at 280 and 260 nm, multi-angle light scattering (MALS), quasi-elastic light scattering (QELS) and refractometer detectors. SAXS frames were collected continuously over the 30-min run at 3s exposures. Subsequent data analyses were performed in BioXTAS RAW (Hopkins *et al.*, 2017) the ATSAS suit. The buffer regions were defined by the SAXS frames prior to the protein elution peak. The subtracted frames were analyzed by Evolving Factor Analysis (Meisburger *et al.*, 2016) to distinguish co-eluted peaks prior to calculating R_g and D_{max}. The R_g was calculated for each of the subtracted frames using the Guinier approximation: $I(q) = I(0) \exp(-q^2Rg^2/3)$ with the limits qRg < 1.3. Shape reconstruction was performed in GASBOR (https://www.embl-hamburg.de/biosaxs/manuals/gasbor.html) with a P62 symmetry constraint, and the averaged envelope is shown.

***In Vitro* Autophosphorylation of CaMKII**

Purify full-length CaMKII (10 ug) was incubated for 10 minutes at room temperature (~22 °C) in reaction buffer containing the following components at their final concentrations: 25 mM Tris (pH 8; Thermo Fisher Scientific), 150 mM KCl (Sigma), 1 mM TCEP (GoldBio), 5% glycerol (Thermo Fisher Scientific), 8 mM $MgCl_2$ (Thermo Fisher Scientific), 2 mM ATP (Sigma), and 6 μM calmodulin. The reaction was quenched with 11 mM EDTA/ 11 mM EGTA then incubated with denaturation buffer (25 mM NH_4HCO_3, 8 M Urea, 10 mM DTT, pH 8) for 15 min at RT. Denatured sample was then alkylated by 20 mM iodoacetamide (1h, RT, dark) and trypsinized (2 ng/uL) overnight at 37 °C. Resulting peptides were mixed with 0.5% TFA, desalted using C18 Cartridge Solid Phase Extraction (Water Corporation), and dried using Speed Vac. Dried peptide was stored at -20 °C until further analysis.

Mass Spectrometric Analysis

The dried peptide was resuspended in 0.1% TFA and resolved using Acclaim PepMap RSLC column C18 2 µm, 100 Å, 15 cm × 75 µm in an Easy nLC 1000 (Thermo Scientific). Solvent A consisted of 0.1% formic acid in water and solvent B, 0.1% formic acid in acetonitrile. Gradient elution profile (300 nL/min) was set as followed: 0 – 90 min, 0 – 35% B; 90 – 95 min, 35 – 95% B; 95 – 110 min, 95% B. Eluted peptides were analyzed on the Orbitrap Fusion mass spectrometer (Thermo Scientific) in data-dependent mode with dynamic exclusion enabled (60 s exclusion time). Full-scan spectra at resolution of 120K (at 200 m/z) were acquired in positive mode over the range of 200 – 1500 m/z, AGC target of 4e5, maximum injection time of 50 ms and 3s cycle time. MS/MS scans were acquired in DDA mode by an orbitrap mass analyzer (HCD, collision energy 30%, resolution 30K, AGC target 5e5, maximum injection time 54 ms, isolation window 1.6 m/z). Thermo Raw files were analyzed in Proteome Discoverer 2.4.1 (Thermo Scientific).

Mass Photometry

MP analyses were carried out with a OneMP mass photometer (Refeyn LTD, Oxford, UK) at room temperature as previously described with minor modifications (Torres-Ocampo *et al.*, 2020). Glass coverslips (cat #630–2105) and gaskets (catalog #CW-50R-1.0) were cleaned with HPLC-grade water and isopropanol and dried under nitrogen gas before use. Gaskets are sealed onto coverslips during the drying process. Fifteen microliters of MP buffer (25 mM Tris pH 8.0, 150 mM KCl) was used to find the camera focus prior to loading the sample onto the gasket. Acquisition camera image size was set to “medium”. A 60-s movie was recorded for each sample in a 512 x 138 pixel at 1kHz frame rate with 0.95-ms exposure time. A standard curve was generated using thyroglobulin (MW 660 kDa), apoferritin (MW 440 kDa), BSA (66.5 kDa) with an error <1%. Proteins were kept at -80 °C until being used. The protein concentration was calculated from absorbance at 280 nm with extinction coefficients of 60850 M^{-1} cm^{-1} (CaMKIIδ) and 66350 M^{-1} cm^{-1} (CaMKIIα). Proteins were diluted from stock concentrations to 1 uM and stored on ice throughout the experiment. Immediately prior to a measurement, proteins were diluted to 400 nM, 300 nM, 200 nM, 100 nM, 50 nM and 5uL at each concentration was applied to 15 uL of the MP buffer preloaded on the gasket to achieve final concentrations of 100 nM, 75 nM, 50 nM, 25 nM, 12.5 nM. Three replicates were performed for each protein at each concentration. Data were analyzed using DiscoverMP software (Refeyn LTD, Oxford, UK).

Crystallization and X-Ray Data Collection

Initial crystallization screening for the full-length CaMKIIδ (D336C) was done using the sitting vapor diffusion method at 20 °C with commercially available screening kits. The D336C mutation was made for another experiment involving chemical labeling the protein. The protein concentration was the same as the protein concentration (19 mg/ml) used to obtain CaMKIIα crystals. Three hits were further optimized by hanging drop vapor diffusion method. Final conditions are listed below. 20% glycerol was included in the cryo-solutions. Diffraction data were obtained at the Advanced Photon Source using Beamline 24-ID-E at 100 K with Eiger 16M detector. Each condition led to different crystal morphology, but they yielded the same crystal space group and unit cell values. Crystallization conditions:

1) 0.1 M pH 6.5 Bis-Tris, 16% PEG 2K, 0.2 M sodium malonate dibasic
2) 0.1 M MES pH 6.5, 1.6 M ammonium sulfate, 10% dioxane
3) 1.675 M Potassium phosphate dibasic/ Sodium phosphate monobasic pH 5.4, 3.35% isopropanol

Data Processing and Structure Determination

Data set was integrated, merged, and scaled using Mosfilm and Pointless within CCP4 suite. The structure was solved by molecular replacement with Phaser (McCoy *et al.*, 2007) using the coordinates of individual CaMKIIδ kinase (PDB: 2VN9) and hub domains (PDB: 2W2C) as

search models. The unit cell volume was big enough to fit three copies of each domain. The regulatory segment and the region until hub domain manually built into clear electron density using Coot and refinement was performed with Refmac5 (Murshudov *et al.*, 1997; Emsley *et al.*, 2010).

Molecular Modeling and Simulation

Loop Modeling

To investigate linker dynamics and minimize computational cost, we chose to include two complete copies of monomers and only the two hub domains of the neighborly packed monomers from the dodecameric CaMKIIδ, which represents the minimal surrounding environment of interested linkers (**Fig. S5**). This construct preserves interactions from four hub domains surrounding two linkers. Overall, four models with different linkers (no linker, exon14, exon18 and reversed exon 18) and the missing loop residues (375-378) were generated using the loop modeling module in the MODELLER software (Sali and Blundell, 1993). The built-in DOPE (Discrete Optimized Protein Energy) score in MODELLER was used to evaluate the energies of the final built models and then those optimized models were visually checked in VMD to assure all loops were closed in both ends with no steric clashes in the side chains. These models and all scripts can be found on Github (https://github.com/kairongdong/camk2_linker_modeling).

Simulation protocol

The above four models were then individually solvated with TIP3P water using the CHARMM-GUI web server (Jo *et al.*, 2008). The systems were neutralized and 200 mM KCl was added. The CHARMM36m force field was used, which has been optimized for both structured and intrinsically disordered proteins (Huang *et al.*, 2017). The final four cubic boxes consist of ~20,000 TIP3P water molecules, ~470 ions, with a total atom of ~210,000 and a cubic box of ~13 nm in size. The energy minimization, equilibration and production were performed with GPU-accelerated GROMACS 2019.4 (Lindahl *et al.*). Each system was first energy-minimized for 500 steps with the steepest descent method and then underwent a 125-ps equilibration simulation under NVT conditions at 300 K, with the protein backbone and sidechain atoms positionally restrained to the reference structure using harmonic force constants of 400 $kJ \cdot mol^{-1} \cdot nm^{-2}$ and 40 $kJ \cdot mol^{-1} \cdot nm^{-2}$, respectively. In the production runs, we used a cutoff of 1.2 nm and a smooth switching function starting at 1.0 nm for calculation of non-boned interactions. The particle mesh Ewald (PME) method was used for long-range electrostatic interactions (Darden *et al.*, 1993). The LINCS algorithm was used to constraint all hydrogen-involving bond lengths (Hess *et al.*, 1997). The Nose-Hoover thermostat was used to maintain system temperature at 400 K (Nosé, 1984; Hoover, 1985). The production simulation of each system was carried out at 400 K under NPT conditions for 200 ns with two parallel runs, during which the Nose-Hoover barostat was used to maintain system pressure isotopically at 1 bar (Parrinello and Rahman, 1981). The temperature of 400 K was used to accelerate the simulation and better probe the difference among various constructs.

Analysis

To investigate the dynamics of linkers and kinase domains in each system, all trajectories were first aligned to their corresponding starting equilibrated structure using the C-alpha of all four hub domains. We then calculated RMSF profiles of all C-alpha atoms of the kinase domains, the

regulatory segments, the linker regions and the hub domains. The RMSF was calculated by averaging the four copies of kinases in the 2 replicas and the error bar shows the standard error. To analyze interactions between the calmodulin-binding segment and the linkers, pairwise distances between C-alpha atoms of residues from the calmodulin-binding sequence (297R and 301K) and spatially adjacent residues from the linkers (the first and last residues of the linker sequence) were calculated. To find out the influence of the dynamics on the interaction between the kinase domain and hub domains, native contact analysis was performed. A cutoff of 4.5 Å was used to define whether a contact between heavy atoms of a pair of residues is formed. The total native contacts number is the number of contacts from the original structure, which was then normalized to be 100%. The native contacts number of each frame was calculated and normalized by the total native contacts number to get the native contact fraction.

REFERENCE

Bayer, KU, Koninck, PD, and Schulman, H (2002). Alternative splicing modulates the frequency-dependent response of CaMKII to Ca2+ oscillations. The EMBO Journal 21, 3590–3597.

Bhattacharyya, M, Karandur, D, and Kuriyan, J (2020). Structural Insights into the Regulation of Ca^{2+} /Calmodulin-Dependent Protein Kinase II (CaMKII). Cold Spring Harb Perspect Biol 12, a035147.

Bhattacharyya, M, Stratton, MM, Going, CC, McSpadden, ED, Huang, Y, Susa, AC, Elleman, A, Cao, YM, Pappireddi, N, Burkhardt, P, *et al.* (2016). Molecular mechanism of activation-triggered subunit exchange in Ca2+/calmodulin-dependent protein kinase II. eLife 5, e13405.

Chao, LH, Pellicena, P, Deindl, S, Barclay, LA, Schulman, H, and Kuriyan, J (2010). Inter-subunit capture of regulatory segments is a component of cooperative CaMKII activation. Nat Struct Mol Biol 17, 264–272.

Chao, LH, Stratton, MM, Lee, I-H, Rosenberg, OS, Levitz, J, Mandell, DJ, Kortemme, T, Groves, JT, Schulman, H, and Kuriyan, J (2011). A Mechanism for Tunable Autoinhibition in the Structure of a Human Ca2+/Calmodulin- Dependent Kinase II Holoenzyme. Cell 146, 732–745.

Chen, X, Cai, Q, Zhou, J, Pleasure, SJ, Schulman, H, Zhang, M, and Nicoll, RA (2023). CaMKII autophosphorylation but not downstream kinase activity is required for synaptic memory. 2023.08.25.554912.

Cook, SG, Bourke, AM, O'Leary, H, Zaegel, V, Lasda, E, Mize-Berge, J, Quillinan, N, Tucker, CL, Coultrap, SJ, Herson, PS, *et al.* (2018). Analysis of the CaMKIIα and β splice-variant distribution among brain regions reveals isoform-specific differences in holoenzyme formation. Sci Rep 8, 5448.

Darden, T, York, D, and Pedersen, L (1993). Particle mesh Ewald: An N·log(N) method for Ewald sums in large systems. The Journal of Chemical Physics 98, 10089–10092.

De Koninck, P, and Schulman, H (1998). Sensitivity of CaM Kinase II to the Frequency of Ca^{2+} Oscillations. Science 279, 227–230.

Emsley, P, Lohkamp, B, Scott, WG, and Cowtan, K (2010). Features and development of Coot. Acta Cryst D 66, 486–501.

Gaertner, TR, Kolodziej, SJ, Wang, D, Kobayashi, R, Koomen, JM, Stoops, JK, and Waxham, MN (2004). Comparative Analyses of the Three-dimensional Structures and Enzymatic Properties of α, β, γ, and δ Isoforms of Ca2+-Calmodulin-dependent Protein Kinase II *. Journal of Biological Chemistry 279, 12484–12494.

Gronenborn, AM (2009). Protein acrobatics in pairs — dimerization via domain swapping. Current Opinion in Structural Biology 19, 39–49.

Heist, EK, Srinivasan, M, and Schulman, H (1998). Phosphorylation at the Nuclear Localization Signal of Ca2+/Calmodulin-dependent Protein Kinase II Blocks Its Nuclear Targeting*. Journal of Biological Chemistry 273, 19763–19771.

Hess, B, Bekker, H, Berendsen, HJC, and Fraaije, JGEM (1997). LINCS: A linear constraint solver for molecular simulations. Journal of Computational Chemistry 18, 1463–1472.

Hoelz, A, Nairn, AC, and Kuriyan, J (2003). Crystal Structure of a Tetradecameric Assembly of the Association Domain of Ca2+/Calmodulin-Dependent Kinase II. Molecular Cell 11, 1241–1251.

Hoover, WG (1985). Canonical dynamics: Equilibrium phase-space distributions. Phys Rev A 31, 1695–1697.

Hopkins, JB, Gillilan, RE, and Skou, S (2017). *BioXTAS RAW*: improvements to a free open-source program for small-angle X-ray scattering data reduction and analysis. J Appl Crystallogr 50, 1545–1553.

Huang, J, Rauscher, S, Nawrocki, G, Ran, T, Feig, M, de Groot, BL, Grubmüller, H, and MacKerell, AD (2017). CHARMM36m: an improved force field for folded and intrinsically disordered proteins. Nat Methods 14, 71–73.

Hura, GL, Menon, AL, Hammel, M, Rambo, RP, Poole II, FL, Tsutakawa, SE, Jenney Jr, FE, Classen, S, Frankel, KA, Hopkins, RC, *et al.* (2009). Robust, high-throughput solution structural analyses by small angle X-ray scattering (SAXS). Nat Methods 6, 606–612.

Jo, S, Kim, T, Iyer, VG, and Im, W (2008). CHARMM-GUI: A web-based graphical user interface for CHARMM. Journal of Computational Chemistry 29, 1859–1865.

Kim, K, Lakhanpal, G, Lu, HE, Khan, M, Suzuki, A, Hayashi, MK, Narayanan, R, Luyben, TT, Matsuda, T, Nagai, T, *et al.* (2015). A Temporary Gating of Actin Remodeling during Synaptic Plasticity Consists of the Interplay between the Kinase and Structural Functions of CaMKII. Neuron 87, 813–826.

Kwiatkowski, AP, and McGill, JM (2000). Alternative Splice Variant of γ-Calmodulin-Dependent Protein Kinase II Alters Activation by Calmodulin. Archives of Biochemistry and Biophysics 378, 377–383.

Lindahl, Abraham, Hess, and van der Spoel GROMACS 2019.4 Manual.

McCoy, AJ, Grosse-Kunstleve, RW, Adams, PD, Winn, MD, Storoni, LC, and Read, RJ (2007). Phaser crystallographic software. Journal of Applied Crystallography 40, 658.

McSpadden, ED, Xia, Z, Chi, CC, Susa, AC, Shah, NH, Gee, CL, Williams, ER, and Kuriyan, J (2019). Variation in assembly stoichiometry in non-metazoan homologs of the hub domain of Ca2+/calmodulin-dependent protein kinase II. Protein Science 28, 1071–1082.

Meisburger, SP, Taylor, AB, Khan, CA, Zhang, S, Fitzpatrick, PF, and Ando, N (2016). Domain Movements upon Activation of Phenylalanine Hydroxylase Characterized by Crystallography and Chromatography-Coupled Small-Angle X-ray Scattering. J Am Chem Soc 138, 6506–6516.

Murshudov, GN, Vagin, AA, and Dodson, EJ (1997). Refinement of Macromolecular Structures by the Maximum-Likelihood Method. Acta Crystallographica Section D 53, 240–255.

Nosé, S (1984). A unified formulation of the constant temperature molecular dynamics methods. The Journal of Chemical Physics 81, 511–519.

O'Leary, H, Lasda, E, and Bayer, KU (2006). CaMKIIᴺ Association with the Actin Cytoskeleton Is Regulated by Alternative Splicing□D. Molecular Biology of the Cell 17, 10.

Özden, C, MacManus, S, Adafia, R, Samkutty, A, Ocampo, AT, Garman, SC, and Stratton, MM (2024). CaMKIIα and CaMKIIβ hub domains adopt distinct oligomeric states and stabilities. 2023.10.09.561517.

Parrinello, M, and Rahman, A (1981). Polymorphic transitions in single crystals: A new molecular dynamics method. Journal of Applied Physics 52, 7182–7190.

Rellos, P, Pike, ACW, Niesen, FH, Salah, E, Lee, WH, Delft, F von, and Knapp, S (2010). Structure of the CaMKIIδ/Calmodulin Complex Reveals the Molecular Mechanism of CaMKII Kinase Activation. PLOS Biology 8, e1000426.

Rich, MT, Abbott, TB, Chung, L, Gulcicek, EE, Stone, KL, Colangelo, CM, Lam, TT, Nairn, AC, Taylor, JR, and Torregrossa, MM (2016). Phosphoproteomic Analysis Reveals a Novel Mechanism of CaMKII Regulation Inversely Induced by Cocaine Memory Extinction versus Reconsolidation. Journal of Neuroscience 36, 7613–7627.

Rosenberg, OS, Deindl, S, Sung, R-J, Nairn, AC, and Kuriyan, J (2005). Structure of the Autoinhibited Kinase Domain of CaMKII and SAXS Analysis of the Holoenzyme. Cell 123, 849–860.

Rousseau, F, Schymkowitz, J, and Itzhaki, LS (2013). Implications of 3D Domain Swapping for Protein Folding, Misfolding and Function. In: Madame Curie Bioscience Database [Internet], Landes Bioscience.

Sali, A, and Blundell, TL (1993). Comparative protein modelling by satisfaction of spatial restraints. J Mol Biol 234, 779–815.

Sloutsky, R, Dziedzic, N, Dunn, MJ, Bates, RM, Torres-Ocampo, AP, Boopathy, S, Page, B, Weeks, JG, Chao, LH, and Stratton, MM (2020). Heterogeneity in human hippocampal CaMKII transcripts reveals allosteric hub-dependent regulation. Sci Signal 13.

Sloutsky, R, and Stratton, MM (2020). Functional implications of CaMKII alternative splicing. European Journal of Neuroscience 54, 6780–6794.

Stratton, M, Lee, I-H, Bhattacharyya, M, Christensen, SM, Chao, LH, Schulman, H, Groves, JT, and Kuriyan, J (2014). Activation-triggered subunit exchange between CaMKII holoenzymes facilitates the spread of kinase activity. eLife 3.

Stratton, MM, Chao, LH, Schulman, H, and Kuriyan, J (2013). Structural studies on the regulation of Ca2+/calmodulin dependent protein kinase II. Current Opinion in Structural Biology 23, 292–301.

Tombes, RM, Faison, MO, and Turbeville, JM (2003). Organization and evolution of multifunctional Ca2+/CaM-dependent protein kinase genes. Gene 322, 17–31.

Torres-Ocampo, AP, Özden, C, Hommer, A, Gardella, A, Lapinskas, E, Samkutty, A, Esposito, E, Garman, SC, and Stratton, MM (2020). Characterization of CaMKIIα holoenzyme stability. Protein Science 29, 1524–1534.

Tullis, JE, Larsen, ME, Rumian, NL, Freund, RK, Boxer, EE, Brown, CN, Coultrap, SJ, Schulman, H, Aoto, J, Dell'Acqua, ML, *et al.* (2023). LTP induction by structural rather than enzymatic functions of CaMKII. Nature 621, 146–153.

Wang, P, Mei, F, Hu, J, Zhu, M, Qi, H, Chen, X, Li, R, McNutt, MA, and Yin, Y (2017). PTENα Modulates CaMKII Signaling and Controls Contextual Fear Memory and Spatial Learning. Cell Reports 19, 2627–2641.

Yang, E, and Schulman, H (1999). Structural examination of autoregulation of multifunctional calcium/calmodulin-dependent protein kinase II. J Biol Chem 274, 26199–26208.

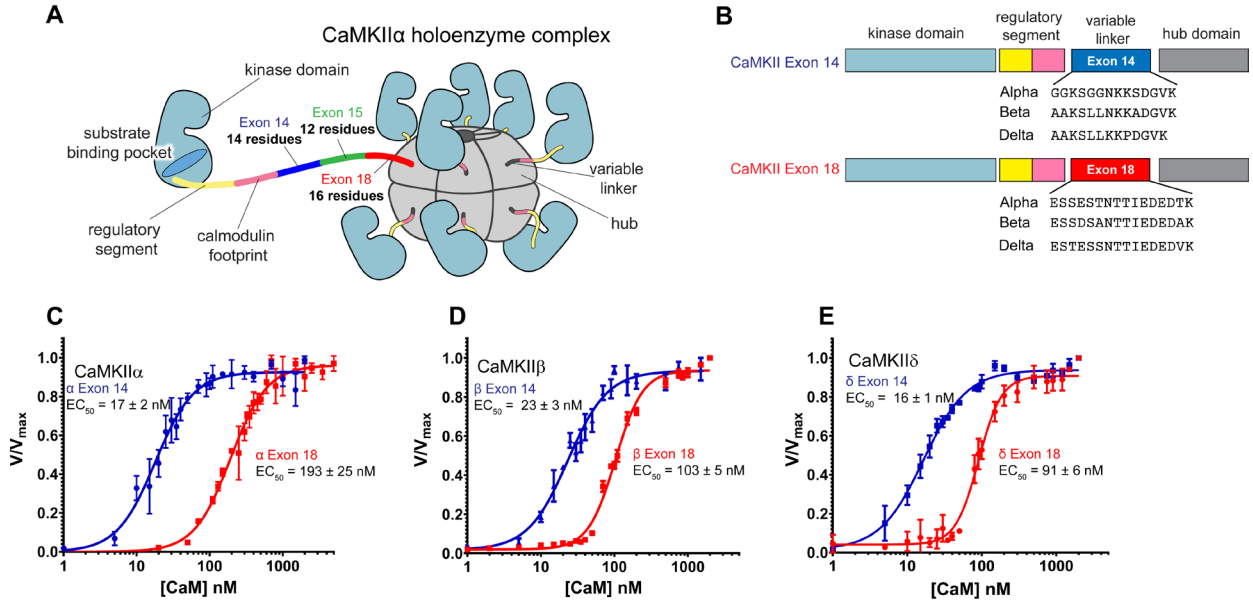

Figure 1. More than the length of the variable linker region affects Ca^{2+}/CaM sensitivity. (A) Overview of CaMKIIα holoenzyme organization containing the linker region that is made of exon 14, exon 15, and exon 18. (B) Subunit architecture and sequences of exon 14 and exon 18 in the variable linker region of CaMKIIα, CaMKIIβ, and CaMKIIδ. (C-E) Kinase assays of CaMKIIα (C), CaMKIIβ (D), and CaMKIIδ (E) comparing the sensitivity to Ca^{2+}/CaM between CaMKII with exon 14 and with exon 18 as the linker region. Each kinase assay comparison was done on the same day. Each data point represents the mean ± SD, n=3.

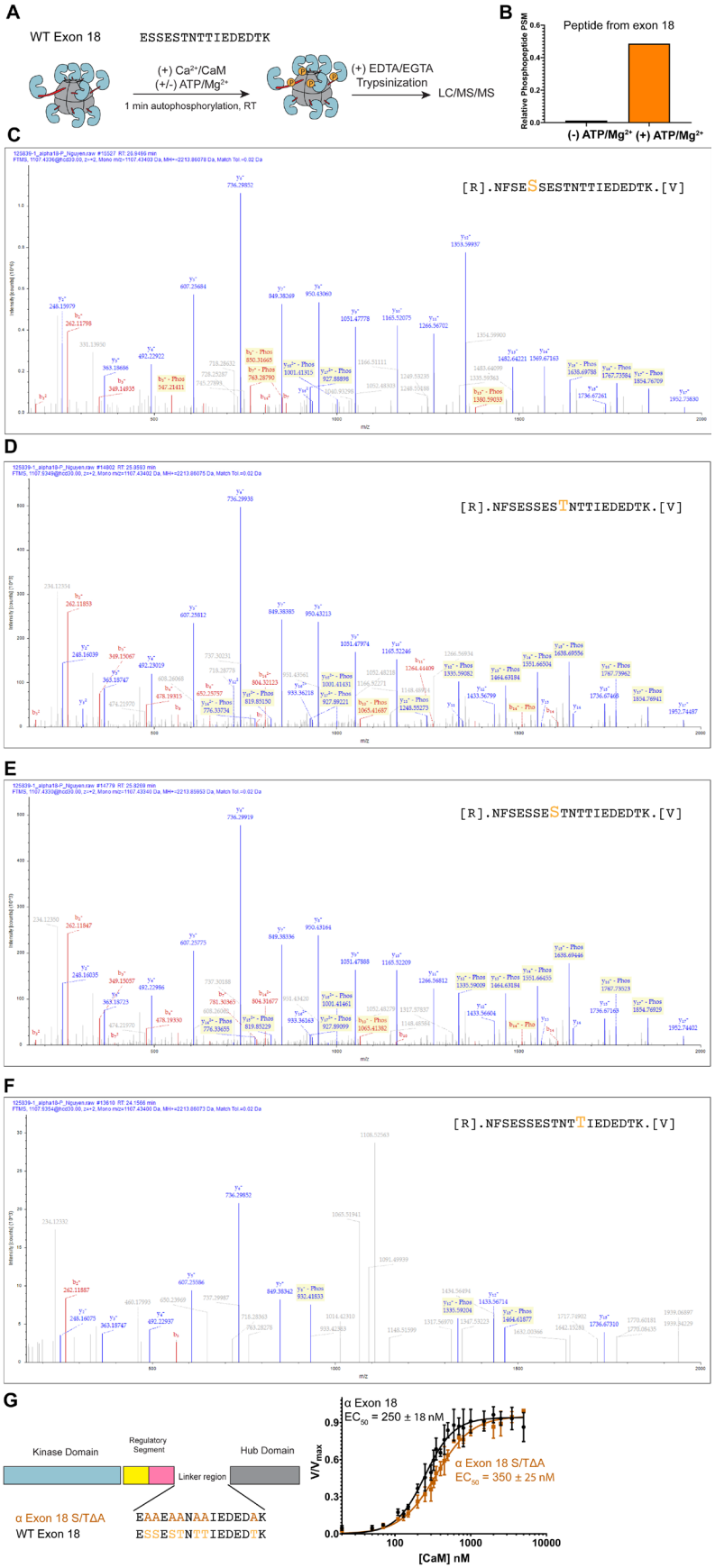
A
WT Exon 18
ESSESTNTTIEDEDTK
(+) Ca2+/CaM
(+/-) ATP/Mg2+
1 min autophosphorylation, RT
(+) EDTA/EGTA
Trypsinization
LC/MS/MS
B
Peptide from exon 18
Relative Phosphopeptide PSM
(-) ATP/Mg2+
(+) ATP/Mg2+
C
[R].NFSESSESTNTTIEDEDTK.[V]
D
[R].NFSESSESTNTTIEDEDTK.[V]
E
[R].NFSESSESTNTTIEDEDTK.[V]
F
[R].NFSESSESTNTTIEDEDTK.[V]
G
Kinase Domain
Regulatory Segment
Hub Domain
Linker region
α Exon 18 S/TΔA
WT Exon 18
EAAEAANAAIEDEDAK
ESSESTNTTIEDEDTK
α Exon 18
EC50 = 250 ± 18 nM
α Exon 18 S/TΔA
EC50 = 350 ± 25 nM
V/Vmax
[CaM] nM

Supplemental Figure 1. Autophosphorylation of exon 18 occurs but does not change Ca^{2+}/CaM sensitivity. (A) Autophosphorylation of exon 18 holoenzyme was carried out at room temperature for 1 minute in the presence of 50 nM CaM, 500 uM Ca^{2+}, 2 mM ATP, 10 mM Mg^{2+}, 25 mM Tris pH 8, 150 mM KCl. The reaction was quenched with 10 mM EGTA/EDTA and processed prior to being submitted to LC/MS/MS. (B) More peptide-spectrum matches (PSMs) of phosphorylated peptides from exon 18 were detected from samples incubated with than that without ATP/Mg^{2+}. Relative PSM was calculated by taking the ratio between phosphorylated peptide PSM and the non-phosphorylated peptide PSM within the same sample. (C-F) Spectra of phosphorylated peptides from exon 18. (G) Kinase assay shows that mutating all Ser and Thr of exon 18 to Ala did not shift the EC_{50} to the left. Each data point of each graph represents the mean ± SD, n=3.

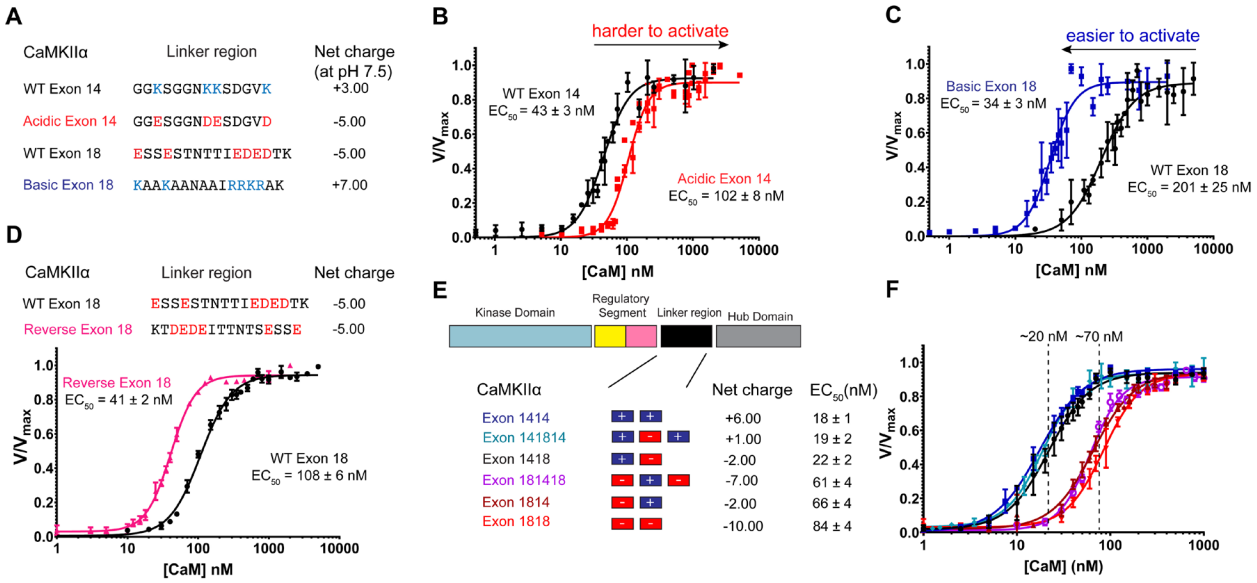

Figure 2. Positions of charged residues on the linker dictate Ca^{2+}/CaM sensitivity. (A) Amino acid sequences of exon 14, exon 18, and the charge-reversal mutants. Basic and acidic residues that are mutated are colored blue and red, respectively. (B-C) CaMKII activity against syntide-2 is tested using linker mutants varying net charge. (D) CaMKII activity against syntide-2 is tested using WT exon 18 and the reverse sequence of exon 18. (E) Cartoon representing combinations of exon 14 and exon 18 used as the CaMKIIα variable linker region. Net charges and EC_{50} values from activity assays shown in (F) are listed. Each kinase assay comparison was done on the same day. Each data point of each graph represents the mean ± SD, n=3.

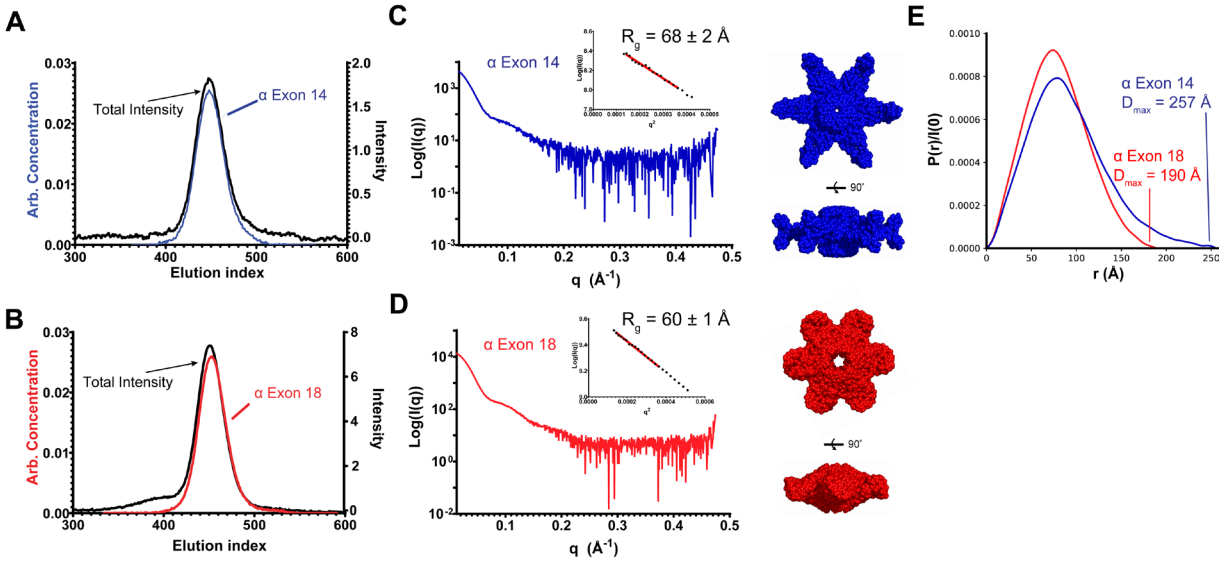

Figure 3. SEC-SAXS reveals a significant shape difference between CaMKIIα containing exon 14 or exon 18. (A-B) Size-exclusion chromatographs of CaMKIIα exon 14 and exon 18 are shown. The protein was monitored with absorbance at 280 nm as shown in black trace. Evolving factor analysis (EFA) indicates the main eluent component under the peak, which is shown for exon 14 (blue) and exon 18 (red). (C-D) SAXS profiles and GASBOR *ab initio* models of CaMKIIα exon 14 and exon 18 are shown in blue (χ^2 = 1.154) and red (χ^2 = 1.307). Insets are the Guinier analysis to interpolate the R_g values for each construct. (E) Pair distance distribution of SAXS profiles of CaMKIIα exon 14 and CaMKIIα exon 18.

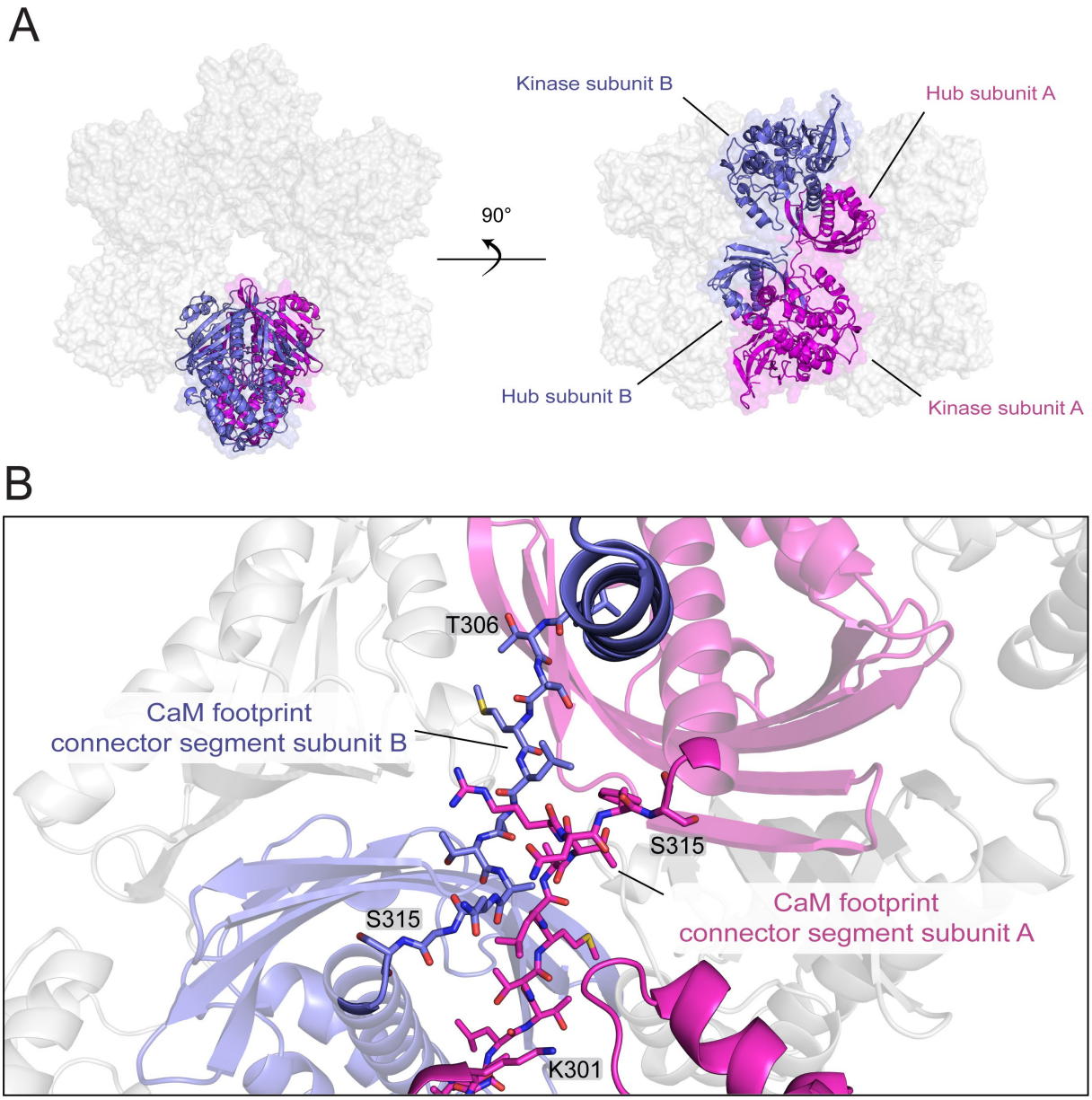

Figure 4. The CaMKIIδ holoenzyme is comprised of domain-swapped dimers. (A) Surface representation of CaMKIIδ holoenzyme crystal structure in two perspectives showing the interaction between the kinase domain of one subunit and the hub domain of another subunit. (B) An overlay of 2Fo-Fc map contoured at 0.8σ showing the connector segments (defined as residues 305-314) in the CaM footprints of two domain-swapping subunits. 2Fo-Fc maps shown are of subunit B (chain C) and subunit A (chain A). The density of R312 sidechain of chain C is missing. The kinase domain of subunit B has been omitted for clarity.

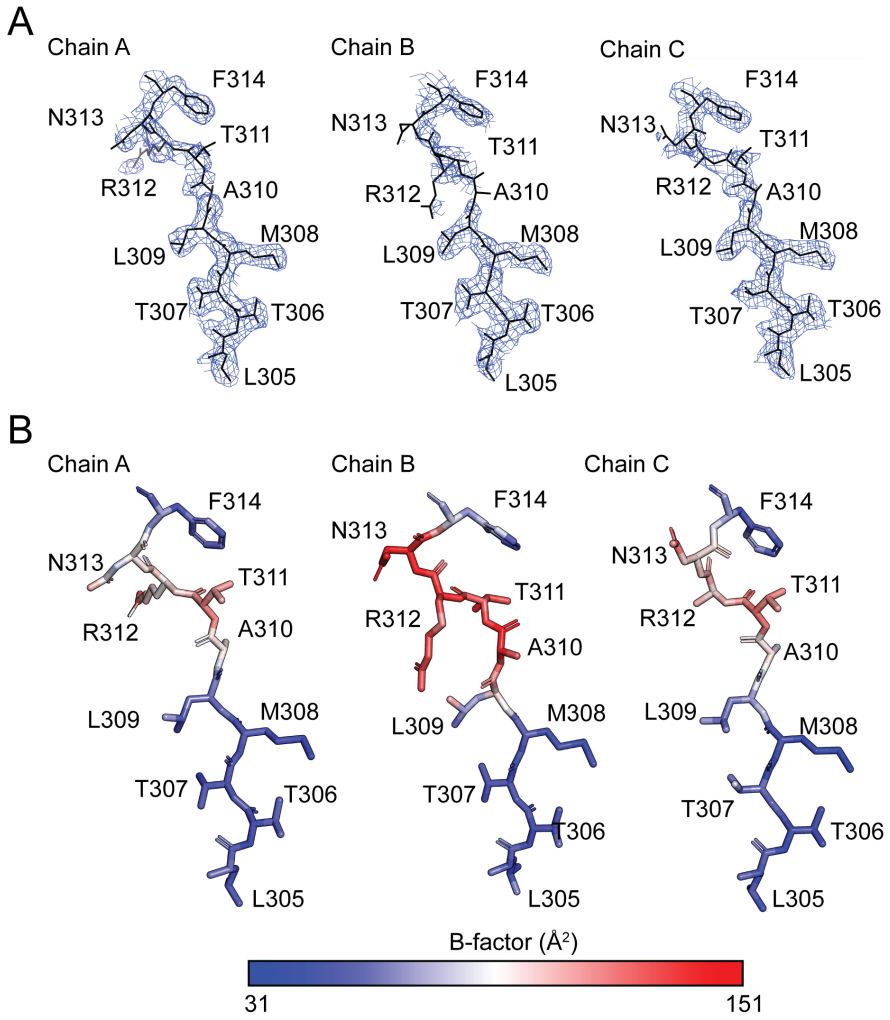

Supplemental Figure 2. Electron density for connector segments. (A) 2Fo-Fc map contoured at 0.7 Å. For all three chains, the electron density is discontinuous for the A310 alpha carbon. (B) Chains colored by B-factor in Pymol. The density of R312 sidechain is missing.

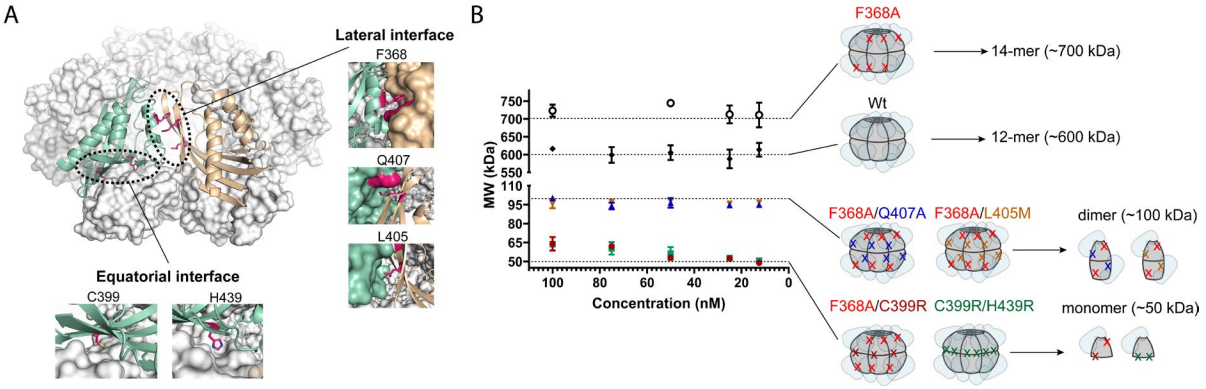

Figure 5. Two mutations are necessary to form predominant dimer or monomer populations. (A) The dodecameric CaMKIIδ hub from the crystal structure presented here is shown with the kinase domains omitted for clarity. Residues highlighted on the right (F368, L405, Q407) are positioned in the lateral hub interface and on the bottom (C399 and H439) are positioned in the equatorial hub interface. (B) Mass photometry analyses at different concentrations of CaMKIIδ holoenzymes with mutations at either or both hub interfaces. Cartoon representations on the right show the positions of the mutations (indicated as X). The kinase domains are translucent for clarity. Data are represented as average molecular weight ± SD (n=3).

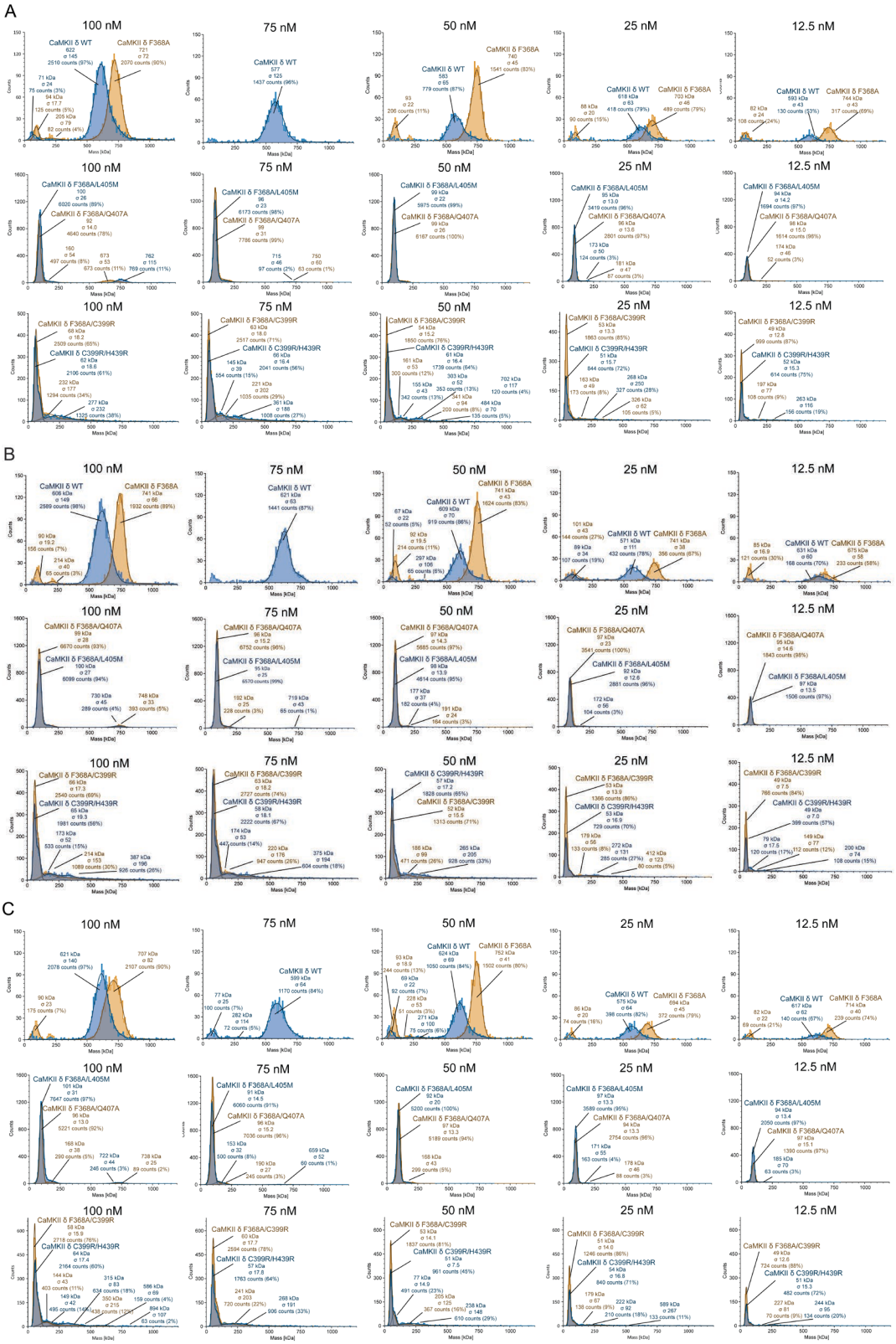

Supplemental Figure 3. Mass photometry data for CaMKIIδ constructs at different concentrations. Each panel represents one replicate.

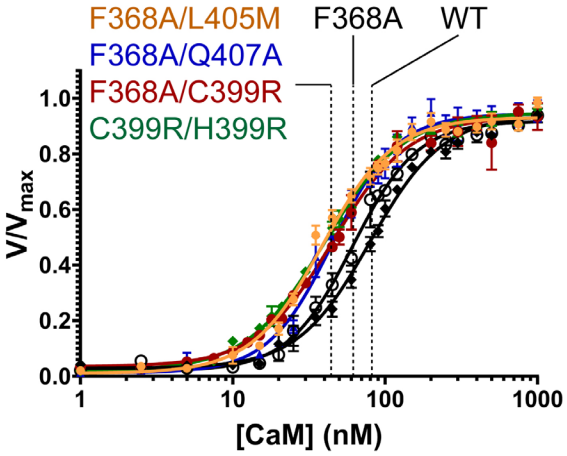

CaMKIIδ no linker	EC_{50} (nM)	h
WT	80 ± 4	1.8 ± 0.2
F368A	61 ± 4	2 ± 0.2
F368A/Q407A	45 ± 3	2 ± 0.2
F368A/L405M	39 ± 3	1.8 ± 0.2
F368A/C399R	45 ± 3	1.7 ± 0.2
C399R/H399R	40 ± 2	1.7 ± 0.1

Supplemental Figure 4. Activity assays of CaMKIIδ wildtype and interface mutants. Activity against syntide-2 was measured over a range of CaM concentrations for the mutants listed. Data are shown as the mean ± SD (n=3).

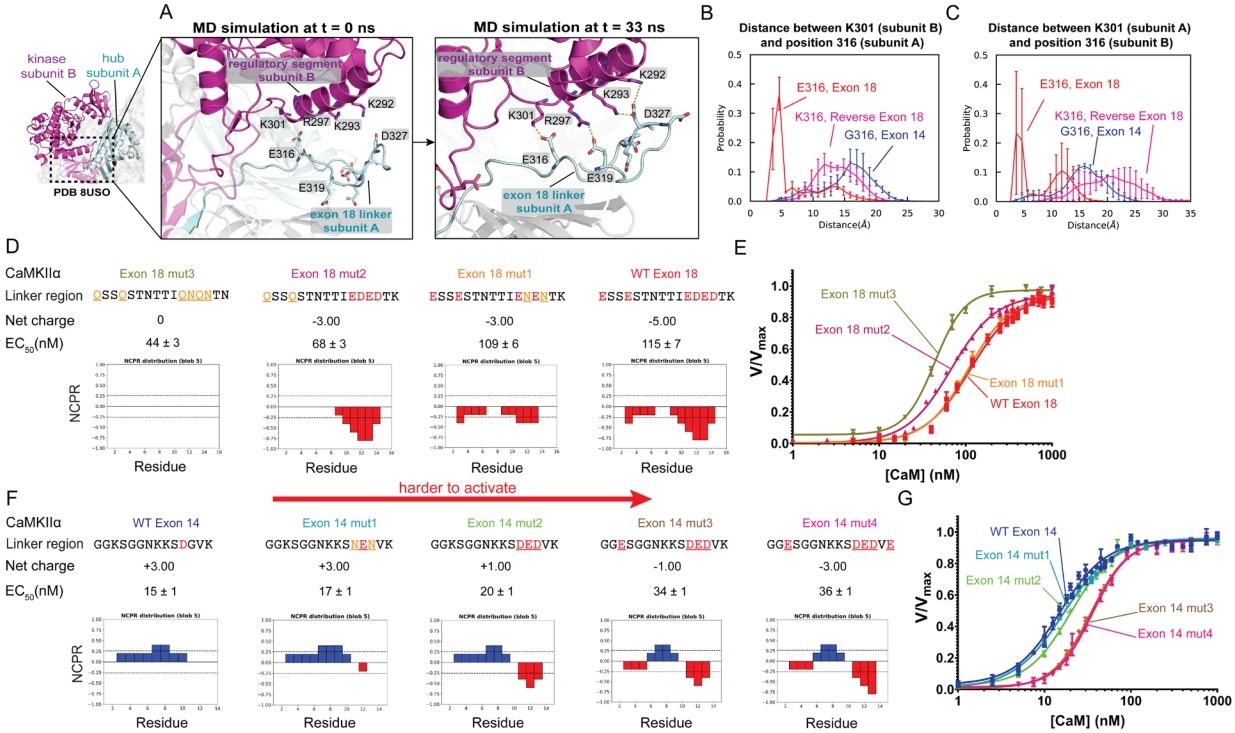

Figure 6. Specific electrostatic interactions between the linker and the calmodulin footprint drive the Ca^{2+}/CaM sensitivity. (A) Snapshots from the MD simulation at time 0 and 33 ns containing the domain-swapped dimer (shown in inset) and exon 18 linker region. Electrostatic interactions are shown using dashed lines in the right panel. (B) Distributions of distance between K301 of subunit B and position 316 of subunit A from simulations of constructs with different linkers as labeled. (C) Same as B except comparing K301 of subunit A and position 316 of subunit B. (D) Sequences of exon 18 mutants are shown to test the position of neutral or charged residues. Net charge and EC_{50} values (see panel E) are shown. (F) Sequences of exon 14 mutants are shown to test the position of neutral or charged residues. Net charge and EC_{50} values (see panel G) are shown. The net charge per residue (NCPR) graphs were plotted using the CIDER server. Data are shown as mean ± SD, n=3.

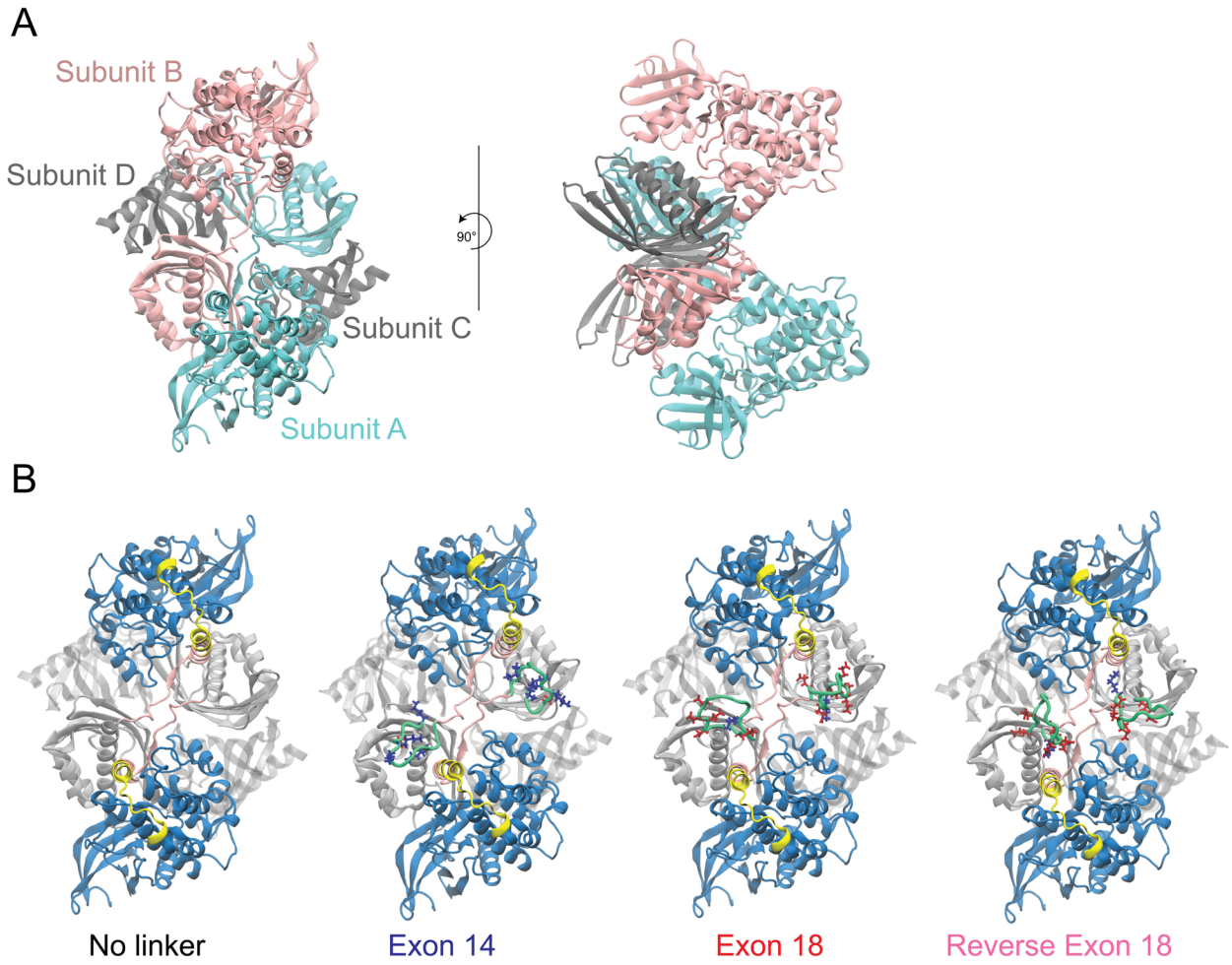

Supplemental Figure 5. CAMKII tetramer for simulation. (A) Tetrameric CaMKII used for linker modeling in MD simulations. This is the smallest unit which houses all possible kinase:hub interactions. Subunits A and B are full-length. Subunits C and D are hub domain one. (B) Tetrameric CaMKIIs with different linker composition. Exon 14, Exon 18, and Reverse Exon 18 were built into the no linker tetramer structure using MODELLER. Kinase: indigo; Regulatory segment: yellow and pink; Calmodulin binding region: pink; hub: gray; linkers: green. The charged residues of the linkers are represented with sticks. Positively charged residues: blue; Negatively charged residues: red.

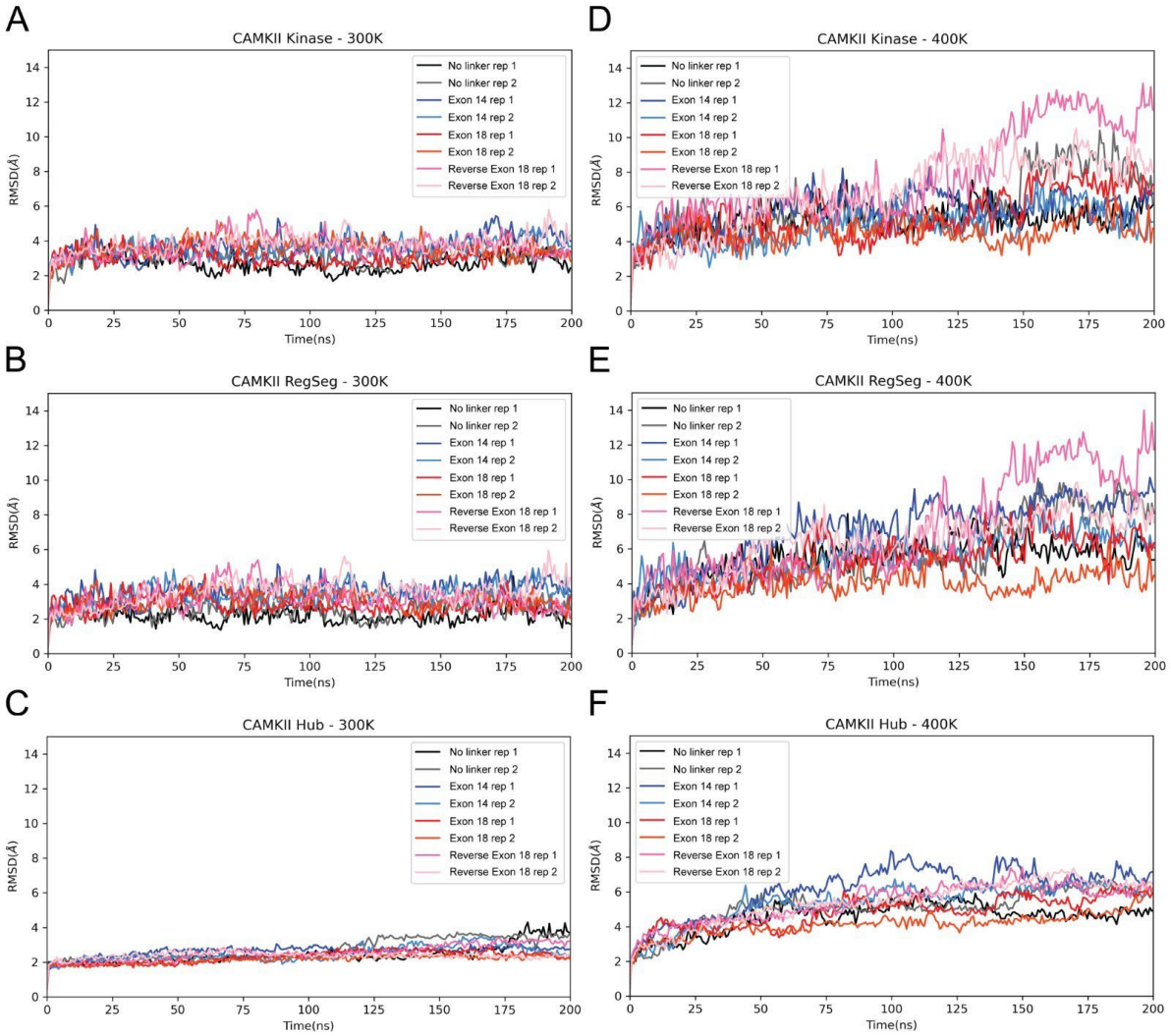

Supplemental Figure 6. CaMKII domains are relatively stable during the 200 ns simulation. (A-C) Root-mean-square deviation (RMSD) was calculated at 300 K for each CaMKII construct and the hub domain was used as the reference in each calculation. (D-F) Same procedure, except the temperature was set to 400 K. Each of the constructs (no linker, Exon 14, Exon 18, and Reverse Exon 18) has two replicas.

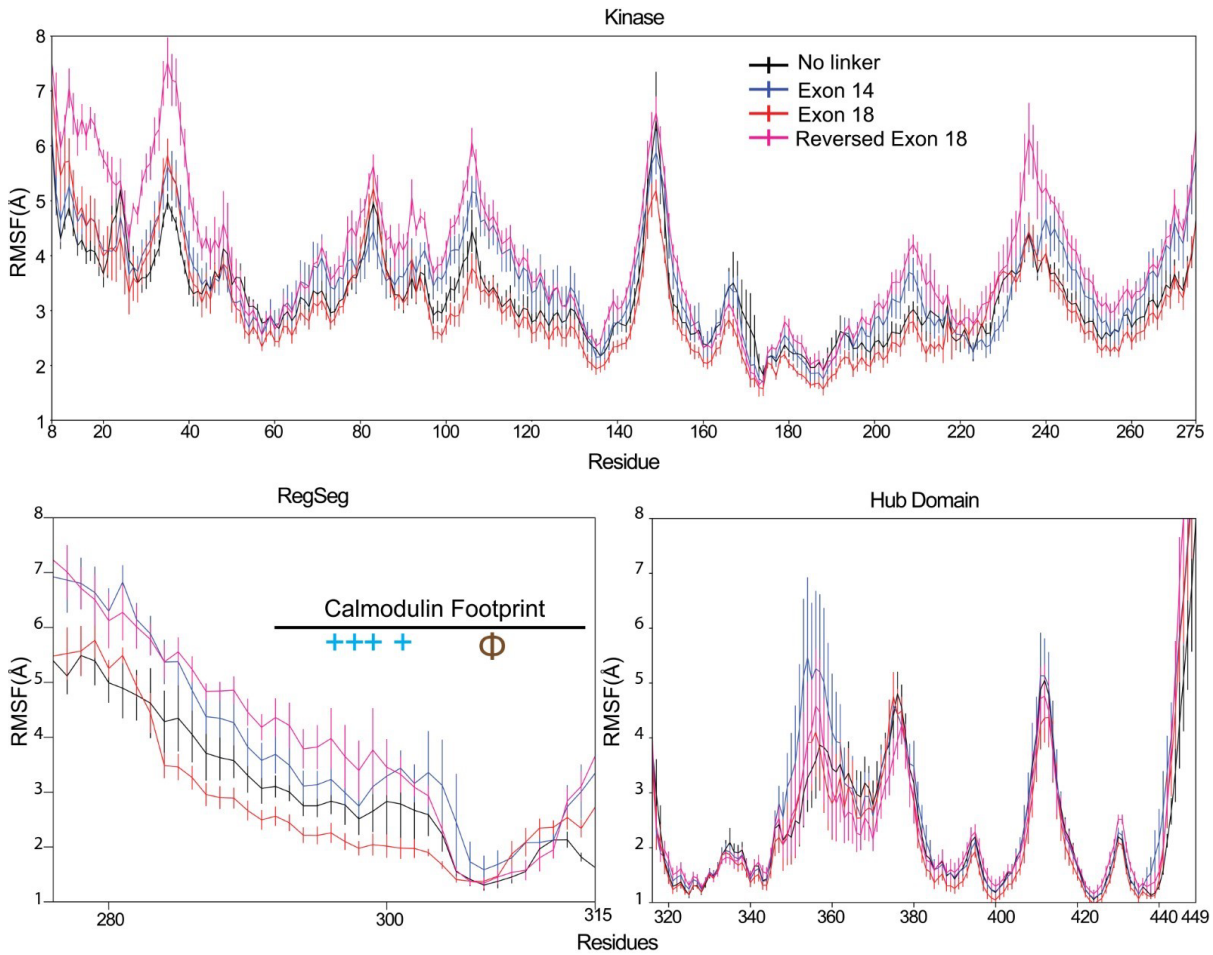

Supplemental Figure 7. **Linker composition alters the fluctuations of the regulatory domain.** RMSF calculation (n = 2) was carried out in the simulations of domain-swapped CaMKII models containing four subunits. On the calmodulin footprint, (+) denotes a positively charged region, and Φ denotes a hydrophobic region.

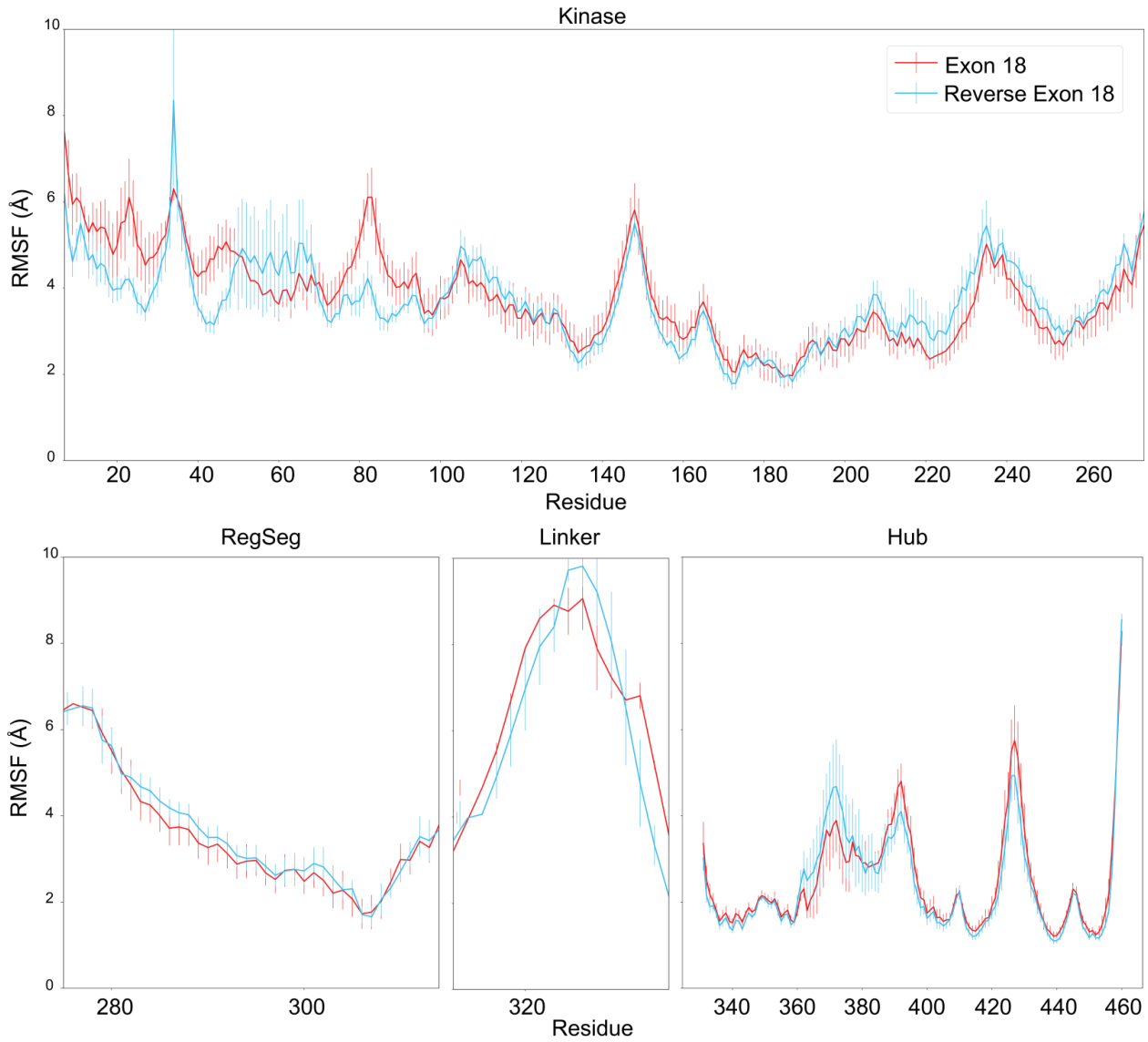

Supplemental Figure 8. **Domain-swapping and linker sequence facilitate regulatory segment dynamics.** In a non-swapped conformation, the differences in RMSF were not observed in between CaMKII Exon 18 and CaMKII Reverse Exon 18 (n=2).

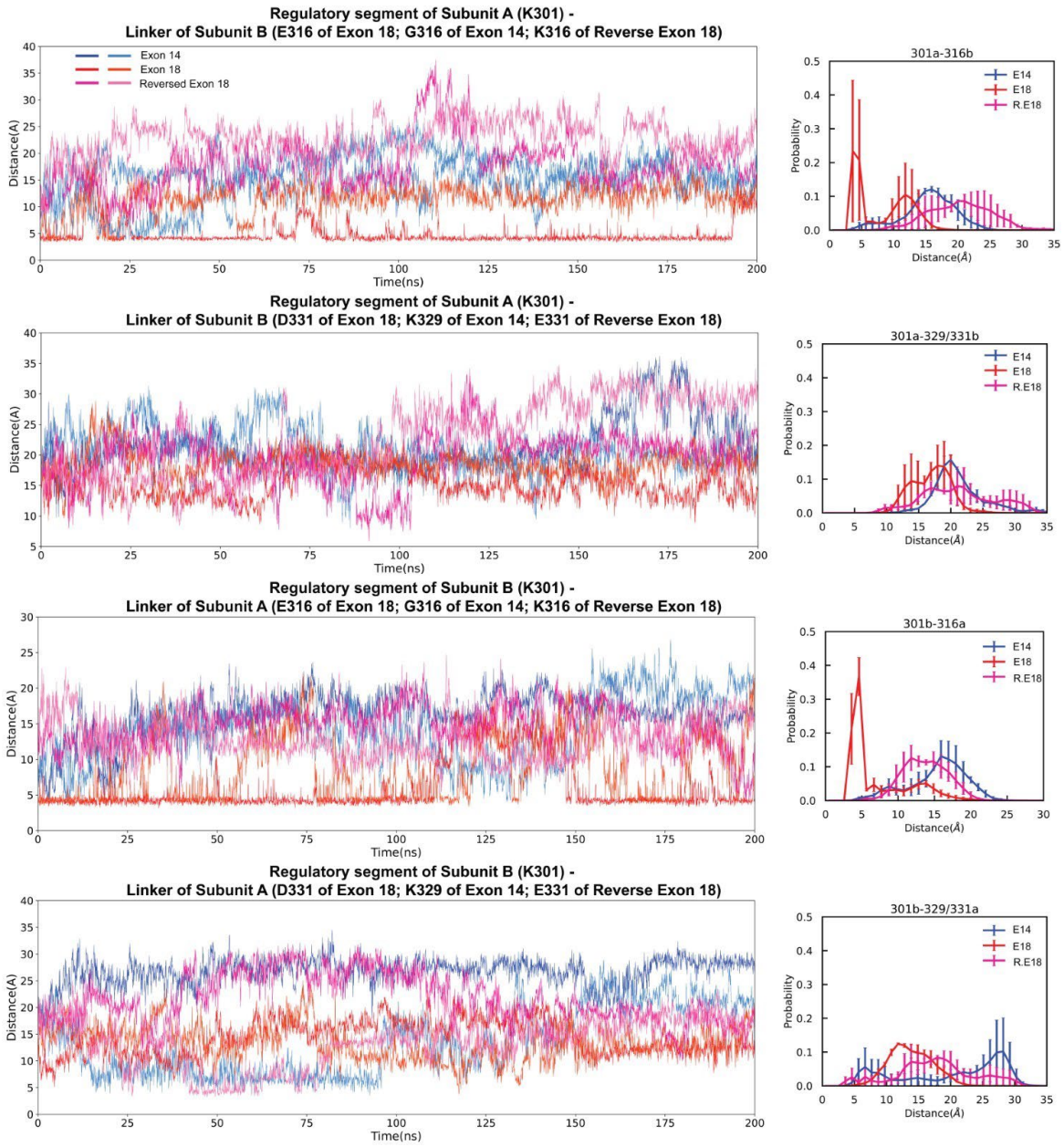

Supplement Figure 9. There is a close interaction between the calmodulin-binding region (K301) and the N-terminal end of the variable linker. Pair-wise interactions are plotted between K301 (calmodulin binding region) and either the N-terminal residue (residue 316) or the C-terminal residue of the linker (residue 329 for exon 14, residue 331 for exon 18 and reversed exon 18) over the 200-ns trajectory. Data from interactions between K301 of chain A and residue 316 of chain B, and vice versa, are shown. The distributions of the distance for each pair of interaction are shown in the right panel (n=2).

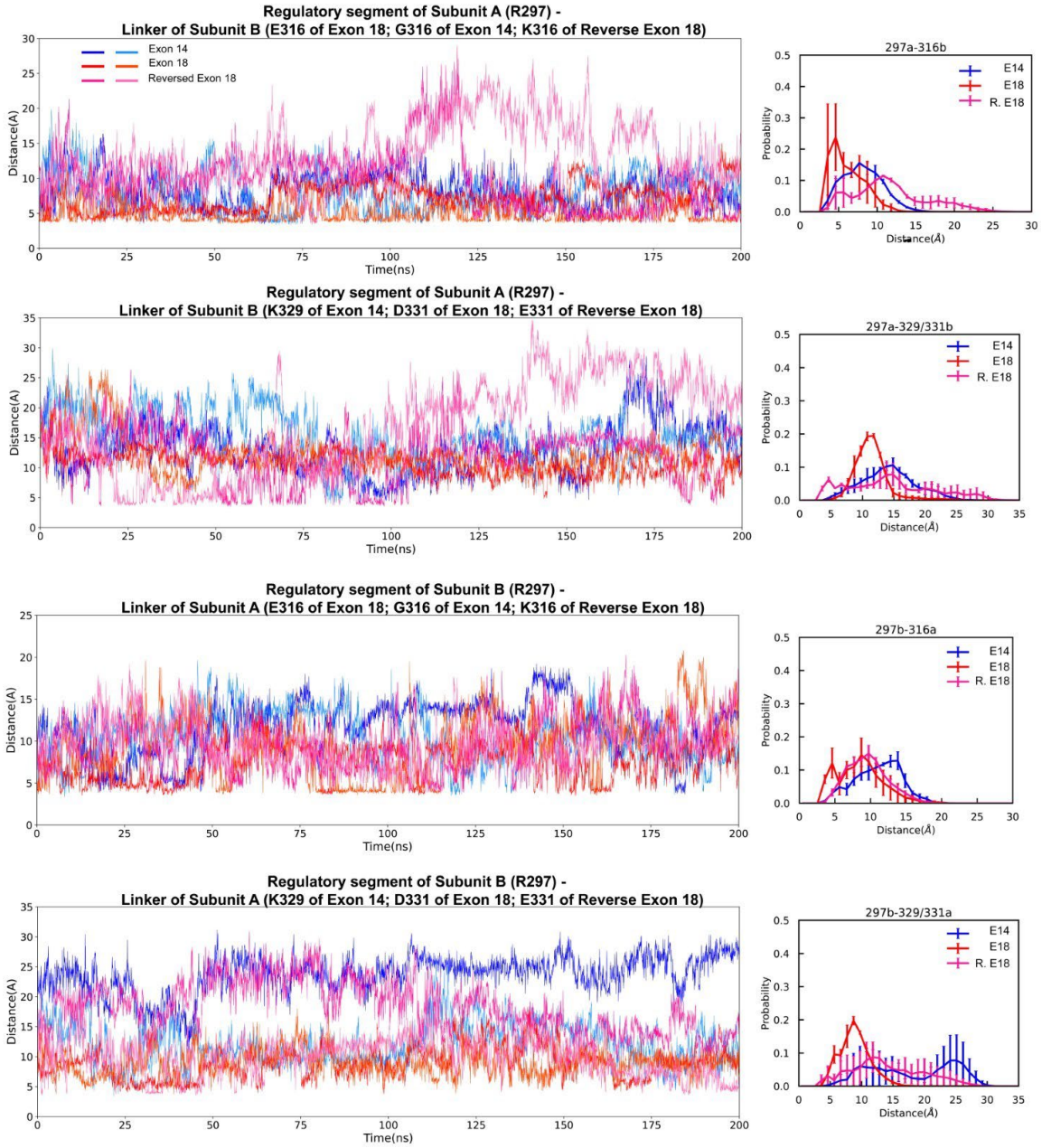

Supplement Figure 10. There is a modest interaction between the calmodulin-binding region (R297) and the N-terminal end of the variable linker. Pair-wise interactions plotted between R297 (calmodulin binding region) and either the N-terminal (residue 316) or C-terminal residue of the linker (residue 329 for exon 14, residue 331 for exon 18 and reversed exon 18) over the 200-ns trajectory. Data from interactions between R297 of chain A and residue 329/331 of chain B, and vice versa, are shown. The distributions of the distance for each pair of interactions are shown in the right panel (n=2).

Table 1. Data Collection and Refinement Statistics

Data collection	
Space group	$P4_222$
Cell dimensions	
a, b, c (Å)	174.984, 174.984, 140.416
α, β, γ (°)	90, 90, 90
Resolution (Å)	50 – 2.3 (2.34 – 2.3)
R_{merge}	0.158 (1.626)
Mean $I/\sigma I$	5.3 (1.4)
Completeness (%)	100.0 (99.9)
Redundancy	20 (12.9)
$CC_{1/2}$	0.997 (0.611)
CC*	0.999 (0.871)
Refinement	
Resolution (Å)	48.53 – 2.3 (2.36 – 2.30)
Unique reflections	86683 (2630)
R_{work} / R_{free} (%)	18.51/21.32
No. atoms	
Protein	10092
Water	274
Ligand	21
Ramachandran plot	
In preferred regions (%)	94.8
In allowed regions (%)	4.7
Outliers (%)	0.5
B-factors	
Protein	50.9
Water	38.2
Ligand	35.0
RMS deviations	
Bond lengths (Å)	0.004
Bond angles (°)	0.73